A free boundary mechanobiological model of epithelial tissues

Tamara A. Tambyah[1], Ryan J. Murphy[1], Pascal R. Buenzli[1] and Matthew J. Simpson[1,*]

[1] *School of Mathematical Sciences, Queensland University of Technology, Brisbane, Australia*

Abstract

In this study, we couple intracellular signalling and cell–based mechanical properties to develop a novel free boundary mechanobiological model of epithelial tissue dynamics. Mechanobiological coupling is introduced at the cell level in a discrete modelling framework, and new reaction–diffusion equations are derived to describe tissue–level outcomes. The free boundary evolves as a result of the underlying biological mechanisms included in the discrete model. To demonstrate the accuracy of the continuum model, we compare numerical solutions from the discrete and continuum models relating to two different signalling pathways. First we study the Rac–Rho pathway where cell– and tissue–level mechanics are directly related to intracellular signalling. We then study an activator–inhibitor system which gives rise to spatial and temporal patterning related to Turing patterns. In all cases, the continuum model and free boundary condition accurately reflect the cell–level processes included in the discrete model.

Key words: moving boundary problem, intracellular signalling, cell–based model, continuum model, reaction–diffusion equations, non-uniform growth

1 Introduction

Epithelial tissues consist of tightly packed monolayers of cells [1–3]. Mechanical cell properties, such as resistance to deformation and cell size, and chemical cell properties, such as intracellular signalling, impact the shape of epithelial tissues [2, 4]. The role of purely mechanical cell properties on tissue dynamics has been studied using mathematical and computational models [5–10]. Other models incorporate intracellular signalling to study its effect on tissue dynamics. [11–15]. We extend these studies by developing a model which couples mechanical cell properties to intracellular signalling. We refer to this as *mechanobiological* coupling. By including mechanobiological coupling in a discrete computational framework, new reaction–diffusion equations are derived to describe how cell–level mechanisms relate to tissue–level outcomes.

Epithelial tissues play important roles in cancer development, wound healing and morphogenesis [2, 16, 17]. Temporal changes in tumour size and wound width in epithelial monolayers can be thought of as the evolution of a free boundary [18, 19]. Many boundary models use a one–phase Stefan condition to describe the evolution of the free boundary [20,21]. Other free boundary models, particularly those used to study biological development, pre-specify the rate of tissue elongation to match experimental observations [22–28]. In this study, we take a different approach by constructing the continuum limit description of a biologically–motivated discrete model. In doing so, we derive a novel free boundary condition that arises from the underlying biological mechanisms included

*Corresponding author: matthew.simpson@qut.edu.au

in the discrete model. While the discrete model is suitable to describe cell–level observations and phenomena [15,29], the continuum limit description is suitable to describe tissue–level dynamics and is more amenable to analysis [30–32].

To confirm the accuracy of the continuum limit description, including the new free boundary condition, we compare the solution of the discrete model with the solution of the continuum model for a homogeneous tissue with no mechanobiological coupling, and observe good correspondence. To investigate mechanobiological coupling within epithelial tissues, the modelling framework is applied in two different case studies. The first case study involves the Rac–Rho pathway where diffusible chemicals called Rho GTPases regulate mechanical cell properties [12,33–38]. We explicitly consider how the coupling between diffusible chemical signals and mechanical properties lead to different tissue–level outcomes, including oscillatory and non-oscillatory tissue dynamics. The second case study involves the diffusion and reaction of an activator–inhibitor system in the context of Turing patterns on a non-uniformly evolving cellular domain [26–28]. In both case studies, the numerical solution of the continuum model provides an accurate description of the underlying discrete mechanisms.

2 Model Description

In this section, we first describe the cell–based model, referred to as the *discrete model*, where mechanical cellular properties are coupled with intracellular signalling. To provide mathematical insight into the discrete model, we then derive the corresponding coarse–grained approximation, which is referred to as the *continuum model*.

2.1 Discrete model

To represent a one dimensional (1D) cross section of epithelial tissue, a 1D chain of cells is considered [8,9] (Figure 1). The tissue length, $L(t)$, evolves in time, while the number of cells, N, remains fixed. We define $x_i(t)$, $i = 0, 1, \ldots N$, to represent the cell boundaries, such that the left boundary of cell i is $x_{i-1}(t)$ and the right boundary of cell i is $x_i(t)$. The left tissue boundary is fixed at $x_0(t) = 0$ and $x_N(t) = L(t)$ is a free boundary.

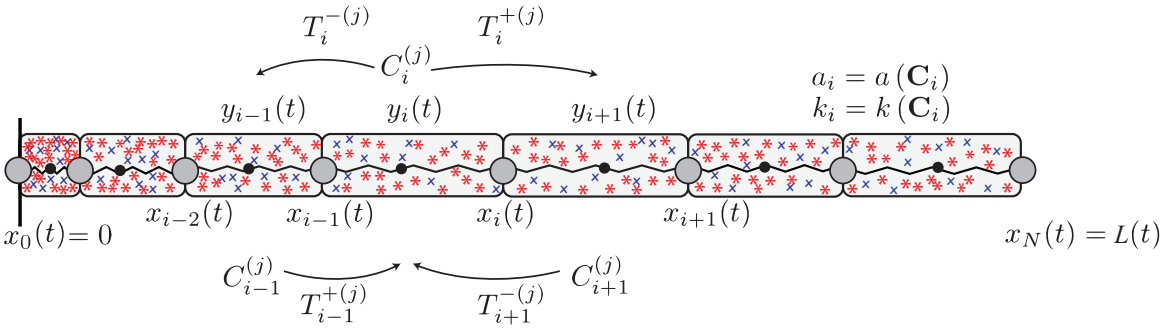

Figure 1: Schematic of the discrete model where mechanical cell properties, a_i and k_i, are functions of the family of chemical signals, $\mathbf{C}_i(t)$. In this schematic we consider two diffusing chemical species where the concentration in the i^{th} cell is $\mathbf{C}_i(t) = \left\{C_i^{(1)}(t), C_i^{(2)}(t)\right\}$. The diffusive flux into cell i from cells $i \pm 1$, and the diffusive flux out of cell i into cells $i \pm 1$ is shown. Cell i, with boundaries at $x_{i-1}(t)$ and $x_i(t)$, is associated with a resident point, $y_i(t)$, that determines the diffusive transport rates, $T_i^{\pm(j)}$.

Each cell, which we consider to be a mechanical spring [8, 9], is assigned potentially distinct mechanical properties, a_i and k_i, such that the resulting tissue is heterogeneous (Figure 1) [7]. Each cell i contains a family of well mixed chemical species, $\mathbf{C}_i(t) = \left\{C_i^{(1)}(t), C_i^{(2)}(t), \ldots, C_i^{(m)}(t)\right\}$, where $C_i^{(j)}(t)$ represents the concentration of the j^{th} chemical species in cell i at time t. As the cell boundaries evolve with time, $C_i^{(j)}(t)$ tends to decrease as cell i expands. Conversely, $C_i^{(j)}(t)$ tends to increase as cell i compresses. Furthermore, $C_i^{(j)}(t)$ diffuses from cell i to cells $i \pm 1$. The mechanical properties of individual cells, such as the cell resting length, $a_i = a\left(\mathbf{C}_i\right)$, and the cell stiffness, $k_i = k\left(\mathbf{C}_i\right)$, may depend on the local chemical concentration, $\mathbf{C}_i(t)$. We refer to this as mechanobiological coupling.

As cells move in overdamped, viscous environments [6, 7, 39], the location of each cell boundary i evolves as

$$\eta \frac{\mathrm{d}x_i}{\mathrm{d}t} = f_{i+1} - f_i, \qquad i = 1, 2, \ldots, N-1, \tag{1}$$

where $\eta > 0$ is the mobility coefficient, and f_i is the cell-to-cell interaction force acting on cell boundary i from the left [6, 7]. For simplicity, we choose a linear, Hookean force law given by

$$f_i = k\left(\mathbf{C}_i\right)\left(x_i(t) - x_{i-1}(t) - a\left(\mathbf{C}_i\right)\right), \qquad i = 1, 2, \ldots, N. \tag{2}$$

The fixed boundary at $x_0(t) = 0$ has zero velocity, whereas the free boundary at $x_N(t) = L(t)$ moves due to the force acting from the left:

$$\eta \frac{\mathrm{d}x_0}{\mathrm{d}t} = 0, \qquad \eta \frac{\mathrm{d}x_N}{\mathrm{d}t} = -f_N. \tag{3}$$

We now formulate a system of ordinary differential equations (ODEs) that describe the rate of change of $C_i^{(j)}(t)$ due to changes in cell length and diffusive transport. A position–jump process is used to describe the diffusive transport of $C_i^{(j)}(t)$. We use $T_i^{\pm(j)}$ to denote the rate of diffusive transport of $C_i^{(j)}(t)$ from cell i to cells $i \pm 1$, respectively [40, 41] (Figure 1). For a standard unbiased position–jump process with a uniform spatial discretisation, linear diffusion at the macroscopic scale is obtained by choosing constant $T_i^{\pm(j)}$ [40]. As the cell boundaries evolve with time, one way to interpret $C_i^{(j)}(t)$ is that it represents a time–dependent, non-uniform spatial discretisation of the concentration profile over the chain of cells. Therefore, care must be taken to specify $T_i^{\pm(j)}$ on the temporally evolving spatial discretisation if we suppose the position–jump process corresponds to linear diffusion at the macroscopic level [41].

Yates et al. [41] show that in order for the position–jump process to lead to linear diffusion at the macroscopic level, the length– and time–dependent transport rates must be chosen as

$$T_i^{-(j)} = \frac{2D_j}{\left(y_i(t) - y_{i-1}(t)\right)\left(y_{i+1}(t) - y_{i-1}(t)\right)}, \qquad i = 2, \ldots, N-1, \tag{4}$$

$$T_i^{+(j)} = \frac{2D_j}{\left(y_{i+1}(t) - y_i(t)\right)\left(y_{i+1}(t) - y_{i-1}(t)\right)}, \qquad i = 2, \ldots, N-1, \tag{5}$$

where $D_j > 0$ is the diffusion coefficient of the j^{th} chemical species at the macroscopic level, and $y_i(t)$ is the *resident point* associated with cell i (Figure 1) [41]. The resident points are a Voronoi partition such that the left jump length for the transport of $C_i^{(j)}(t)$ is $y_i(t) - y_{i-1}(t)$, and the right jump length for the transport of $C_i^{(j)}(t)$ is $y_{i+1}(t) - y_i(t)$ [41]. Complete details of defining a Voronoi partition are outlined in Appendix B.1.1.

At the tissue boundaries, we set $T_1^{-(j)} = T_N^{+(j)} = 0$ so that the flux of $C_1^{(j)}(t)$ and $C_N^{(j)}(t)$ across $x_0(t) = 0$ and $x_N(t) = L(t)$ is identically zero at all times. We follow Yates et al. [41] and choose the inward jump length for the transport of $C_1^{(j)}(t)$ and $C_N^{(j)}(t)$ as $2\left(y_1(t) - x_0(t)\right)$ and $2\left(x_N(t) - y_N(t)\right)$, respectively, giving

$$T_1^{+(j)} = \frac{2D_j}{\left(y_2(t) - y_1(t)\right)\left(y_2(t) + y_1(t)\right)}, \tag{6}$$

$$T_N^{-(j)} = \frac{2D_j}{\left(y_N(t) - y_{N-1}(t)\right)\left(x_N(t) - y_N(t) - y_{N-1}(t)\right)}. \tag{7}$$

Therefore, the ODEs which describe the evolution of $C_i^{(j)}(t)$ are:

$$\frac{\mathrm{d}C_1^{(j)}}{\mathrm{d}t} = \underbrace{Z^{(j)}\left(\mathbf{C}_1\right)}_{\substack{\text{chemical}\\ \text{reactions}}} - \underbrace{\frac{C_1^{(j)}}{l_1}\frac{\mathrm{d}l_1}{\mathrm{d}t}}_{\substack{\text{changes in}\\ \text{cell length}}} + \frac{1}{l_1}\left(\underbrace{T_2^{-(j)} C_2^{(j)} l_2}_{\substack{\text{diffusion into}\\ \text{cell 1}}} - \underbrace{T_1^{+(j)} C_1^{(j)} l_1}_{\substack{\text{diffusion out of}\\ \text{cell 1}}} \right), \tag{8}$$

$$\begin{aligned}\frac{\mathrm{d}C_i^{(j)}}{\mathrm{d}t} &= \underbrace{Z^{(j)}\left(\mathbf{C}_i\right)}_{\substack{\text{chemical}\\ \text{reactions}}} - \underbrace{\frac{C_i^{(j)}}{l_i}\frac{\mathrm{d}l_i}{\mathrm{d}t}}_{\substack{\text{changes in}\\ \text{cell length}}} \\ &+ \frac{1}{l_i}\left(\underbrace{T_{i-1}^{+(j)} C_{i-1}^{(j)} l_{i-1} + T_{i+1}^{-(j)} C_{i+1}^{(j)} l_{i+1}}_{\text{diffusion into cell } i} - \underbrace{\left(T_i^{+(j)} + T_i^{-(j)}\right) C_i^{(j)} l_i}_{\text{diffusion out of cell } i} \right), \quad i = 2, \ldots, N-1,\end{aligned} \tag{9}$$

$$\frac{\mathrm{d}C_N^{(j)}}{\mathrm{d}t} = \underbrace{Z^{(j)}\left(\mathbf{C}_N\right)}_{\substack{\text{chemical}\\ \text{reactions}}} - \underbrace{\frac{C_N^{(j)}}{l_N}\frac{\mathrm{d}l_N}{\mathrm{d}t}}_{\substack{\text{changes in}\\ \text{cell length}}} + \frac{1}{l_N}\left(\underbrace{T_{N-1}^{+(j)} C_{N-1}^{(j)} l_{N-1}}_{\substack{\text{diffusion into}\\ \text{cell } N}} - \underbrace{T_N^{-(j)} C_N^{(j)} l_N}_{\substack{\text{diffusion out of}\\ \text{cell } N}} \right), \tag{10}$$

where $l_i = x_i(t) - x_{i-1}(t)$ is the length of cell i. Chemical reactions between the chemical species residing in the i^{th} cell are described by $Z^{(j)}\left(\mathbf{C}_i\right)$. The form of $Z^{(j)}\left(\mathbf{C}_i\right)$ is chosen to correspond to different signalling pathways.

In summary, the discrete model is given by Equations (1)–(10), where Equations (1)–(3) describe the mechanical interaction of cells, and Equations (8)–(10) describe the underlying biological mechanisms. We solve this deterministic system of ODEs numerically using `ode15s` in MATLAB [42]. The numerical method is outlined in Appendix B.1, and key numerical algorithms are available on GitHub.

2.2 Continuum model

Assuming that the tissue consists of a sufficiently large number of individual cells, N, we now derive an approximate continuum limit description of the discrete model. The discrete model describes the mechanical relaxation of cells, chemical reactions within cells, and diffusive transport between nearest neighbour cells. To keep the derivation of the continuum model as straightforward as possible, we first consider the continuum limit description of the reactions terms, and then consider the continuum limit description of the transport terms.

In the discrete model, $i = 0, 1, \ldots, N$ is a discrete variable which indexes cell positions and cell properties. The time evolution of the cell boundaries, $x_i(t)$, is a set of $N+1$ discrete functions that depend continuously upon time. In contrast, the continuum model describes the spatially continuous evolution of cell boundary trajectories in terms of the cell density per unit length, $q(x,t)$.

In the continuum model, we consider $\bar{i} = i/N$ as the continuous analogue of i [5]. As $N \to \infty$, $\bar{i} = 0, 1/N, \ldots, 1$ becomes a continuous variable and defines a continuum of cells. The spatially and temporally continuous cell density is [5, 8]

$$q(x,t) = N\frac{\partial \bar{i}(x,t)}{\partial x}, \qquad x \in [0, L(t)] \text{ and } \bar{i} \in [0,1]. \tag{11}$$

For each time t, $x(\bar{i},t)$ is defined as the inverse function of $\bar{i}(x,t)$ where $0 \leq x \leq L(t)$ for $\bar{i} \in [0,1]$. We use $x(\bar{i},t)$ to represent the continuous spatial and temporal evolution of cell boundary trajectories [5].

The discrete quantity $\mathbf{C}_i(t)$ becomes a multicomponent vector field in the continuum model, $\boldsymbol{\mathcal{C}}(x,t) = \{\mathcal{C}_1(x,t), \mathcal{C}_2(x,t), \ldots, \mathcal{C}_m(x,t)\}$. We assume that the mechanical relaxation of cells is sufficiently fast such that the spatial distribution of cell lengths is slowly varying in space [6]. Under this assumption, the location of the resident points can be approximated as the midpoint of each cell. Thus,

$$\mathcal{C}_j\left(x\left(\frac{i}{N} - \frac{1}{2N}, t\right), t\right) = C_i^{(j)}(t), \qquad i = 1, \ldots, N. \tag{12}$$

In Equation (12), the subscript j denotes the j^{th} chemical species in the continuum model, and the superscript (j) denotes the j^{th} chemical species in the discrete analogue. Mechanobiological coupling is introduced by allowing the cell stiffness, $k\left(\boldsymbol{\mathcal{C}}\right)$, and the cell resting length, $a\left(\boldsymbol{\mathcal{C}}\right)$, to depend on the chemical family.

We write the linear force law for the continuum of cells as

$$f\left(\bar{i},t\right) = k\left(\boldsymbol{\mathcal{C}}\right)\left(x\left(\bar{i},t\right) - x\left(\bar{i} - 1/N, t\right) - a\left(\boldsymbol{\mathcal{C}}\right)\right), \tag{13}$$

where $\boldsymbol{\mathcal{C}}$ is evaluated at $\bar{i} - 1/(2N)$ in Equation (13). Thus, the equations of motion are:

$$\eta\frac{\partial x(\bar{i},t)}{\partial t} = 0, \qquad \bar{i} = 0, \tag{14}$$

$$\eta\frac{\partial x(\bar{i},t)}{\partial t} = f\left(\bar{i} + 1/N, t\right) - f\left(\bar{i},t\right), \qquad \bar{i} \in (1/N, 1), \tag{15}$$

$$\eta\frac{\partial x(\bar{i},t)}{\partial t} = -f\left(\bar{i},t\right), \qquad \bar{i} = 1. \tag{16}$$

The definition of $f(\bar{i},t)$ in Equation (13) contains arguments evaluated at $\bar{i}$, $\bar{i} - 1/N$ and $\bar{i} - 1/(2N)$. Equation (13) is substituted into Equations (14)–(16), and all components are expanded in a Taylor series about $\bar{i}$ as $N \to \infty$,

$$\eta\frac{\partial x}{\partial t} = 0, \qquad \bar{i} = 0, \tag{17}$$

$$\eta\frac{\partial x}{\partial t} = -\frac{a}{N}\frac{\partial k}{\partial \bar{i}} - \frac{k}{N}\frac{\partial a}{\partial \bar{i}} + \frac{1}{N^2}\frac{\partial x}{\partial \bar{i}}\frac{\partial k}{\partial \bar{i}} + \frac{k}{N^2}\frac{\partial^2 x}{\partial \bar{i}^2} + \mathcal{O}\left(N^{-3}\right), \qquad \bar{i} \in (1/N, 1), \tag{18}$$

$$\eta\frac{\partial x}{\partial t} = ak - \frac{k}{N}\frac{\partial x}{\partial \bar{i}} - \frac{k}{2N}\frac{\partial a}{\partial \bar{i}} - \frac{a}{2N}\frac{\partial k}{\partial \bar{i}} + \frac{1}{2N^2}\frac{\partial k}{\partial \bar{i}}\frac{\partial x}{\partial \bar{i}} + \frac{k}{2N^2}\frac{\partial^2 x}{\partial \bar{i}^2},$$
$$+ \frac{k}{4N^2}\frac{\partial^2 a}{\partial \bar{i}^2} + \frac{a}{4N^2}\frac{\partial^2 k}{\partial \bar{i}^2} + \frac{1}{4N^2}\frac{\partial k}{\partial \bar{i}}\frac{\partial a}{\partial \bar{i}} + \mathcal{O}\left(N^{-3}\right), \qquad \bar{i} = 1. \tag{19}$$

To describe the continuous evolution of cell trajectories and cell properties, we relate the cell length to the inverse of cell density [6, 7], and define the continuous linear force law corresponding

to Equation (13) as a 1D stress field,

$$f(x,t) = k\left(\boldsymbol{\mathcal{C}}(x,t)\right)\left(\frac{1}{q(x,t)} - a\left(\boldsymbol{\mathcal{C}}(x,t)\right)\right), \qquad x \in \left(0, L\left(t\right)\right). \tag{20}$$

We express Equations (17)–(19) in terms of $q(x,t)$ and $f(x,t)$ through a change of variables from $(\bar{i},t)$ to (x,t) [5,8]. The change of variables gives

$$\frac{\partial x}{\partial \bar{i}} = \frac{N}{q}, \qquad \frac{\partial x}{\partial t} = -\frac{N}{q}\frac{\partial \bar{i}}{\partial t}, \tag{21}$$

$$\frac{\partial k}{\partial \bar{i}} = \frac{\partial k}{\partial x}\frac{\partial x}{\partial \bar{i}} = \frac{N}{q}\frac{\partial k}{\partial x}, \qquad \frac{\partial a}{\partial \bar{i}} = \frac{\partial a}{\partial x}\frac{\partial x}{\partial \bar{i}} = \frac{N}{q}\frac{\partial a}{\partial x}. \tag{22}$$

Complete details of the change of variables calculation are outlined in Appendix A.1. The non-zero $\mathcal{O}\left(N^{-3}\right)$ terms are neglected in Equations (17)–(19) and we show in Section 3 that the truncated Taylor series expansion is sufficient to ensure reasonably good agreement between solutions of the discrete and continuum models.

The local cell velocity, $u(x,t) = \partial x/\partial t$, is derived by substituting Equations (21)–(22) into the right hand side of Equation (18). Factorising in terms of $f(x,t)$ gives,

$$u(x,t) = \frac{1}{\eta q(x,t)}\frac{\partial f(x,t)}{\partial x}, \qquad x \in \left(0, L\left(t\right)\right). \tag{23}$$

As $u(x,t) = \partial x/\partial t$, we substitute Equation (21) into the left hand side of Equation (23) to derive the governing equation for cell density. The resulting equation is differentiated with respect to x to give,

$$\frac{\partial}{\partial x}\left(N\frac{\partial \bar{i}}{\partial t}\right) = \frac{\partial}{\partial x}\left(-\frac{1}{\eta}\frac{\partial f(x,t)}{\partial x}\right), \qquad x \in \left(0, L\left(t\right)\right). \tag{24}$$

The order of differentiation on the left hand side of Equation (24) is reversed, and Equation (21) is used [5,8] to give,

$$\frac{\partial q(x,t)}{\partial t} = -\frac{1}{\eta}\frac{\partial^2 f(x,t)}{\partial x^2}, \qquad x \in \left(0, L\left(t\right)\right). \tag{25}$$

We now derive the boundary condition for the evolution of $L(t)$ by substituting Equations (21)–(22) into the right hand side of Equation (19), giving

$$\begin{aligned}\eta\,\frac{\partial x}{\partial t} &= ak - \frac{k}{q} - \frac{k}{2q^3}\frac{\partial q}{\partial x} + \frac{1}{2q^2}\frac{\partial k}{\partial x} - \frac{1}{2q}\frac{\partial}{\partial x}(ak)\\ &\quad + \frac{1}{4q}\left\{\frac{1}{q}\frac{\partial a}{\partial x}\frac{\partial k}{\partial x} + k\frac{\partial}{\partial x}\left(\frac{1}{q}\frac{\partial a}{\partial x}\right) + a\frac{\partial}{\partial x}\left(\frac{1}{q}\frac{\partial k}{\partial x}\right)\right\}, \qquad x = L(t).\end{aligned} \tag{26}$$

As $u(x,t) = \partial x/\partial t$, the left hand side of Equation (26) is equated to Equation (23). Factorising in terms of $f(x,t)$ gives the free boundary condition

$$\begin{aligned}0 = f(x,t) &+ \frac{1}{2q(x,t)}\frac{\partial f(x,t)}{\partial x} + \frac{1}{4q(x,t)}\left\{\frac{1}{q(x,t)}\frac{\partial a\left(\boldsymbol{\mathcal{C}}(x,t)\right)}{\partial x}\frac{\partial k\left(\boldsymbol{\mathcal{C}}(x,t)\right)}{\partial x}\right.\\ &\left. + k\left(\boldsymbol{\mathcal{C}}(x,t)\right)\frac{\partial}{\partial x}\left(\frac{1}{q(x,t)}\frac{\partial a\left(\boldsymbol{\mathcal{C}}(x,t)\right)}{\partial x}\right) + a\left(\boldsymbol{\mathcal{C}}(x,t)\right)\frac{\partial}{\partial x}\left(\frac{1}{q(x,t)}\frac{\partial k\left(\boldsymbol{\mathcal{C}}(x,t)\right)}{\partial x}\right)\right\}, \quad x = L(t).\end{aligned} \tag{27}$$

A similar transformation is applied to Equation (17) to yield the left boundary condition as

$$\frac{\partial f(x,t)}{\partial x} = 0, \qquad x = 0. \tag{28}$$

Equations (23), (25), (27) and (28) form a continuum limit approximation of the discrete model.

Equations (23), (25) and (28) were reported previously by Murphy et al. [6] who consider tissues of fixed length. A key contribution here is the derivation of Equation (27), which describes how the free boundary evolves due to the underlying biological mechanisms and heterogeneity included in the discrete model. For a homogeneous tissue where the cell stiffness and cell resting length are constant and independent of $\mathcal{C}_j(x,t)$, Equation (27) is equivalent to Equation (23) in Baker et al. [5]. Appendix A.2 shows that Equations (23), (25) and (28) can be derived without expanding all components of Equations (14)–(15). As the definition of $f(\bar{i},t)$ in Equation (13) contains arguments evaluated at $\bar{i}$, $\bar{i}-1/N$ and $\bar{i}-1/(2N)$, it is necessary to expand all components of Equation (16) about $\bar{i}$ to derive Equation (27). For consistency, Equations (23), (25) and (28) are derived in the same way. Numerical exploration in Section 3 reveals that solutions of Equations (23), (25), (27) and (28) accurately reflect the solution of the discrete model.

We now derive a reaction–diffusion equation for the evolution of $\mathcal{C}_j(x,t)$. The reaction–diffusion equation involves terms associated with the material derivative, diffusive transport, and source terms that reflect chemical reactions as well as the effects of changes in cell length,

$$\underbrace{\frac{\partial \mathcal{C}_j(x,t)}{\partial t} + u(x,t)\frac{\partial \mathcal{C}_j(x,t)}{\partial x}}_{\text{material derivative}} + \underbrace{\mathcal{C}_j(x,t)\frac{\partial u(x,t)}{\partial x}}_{\text{changes in cell length}} - \underbrace{D_j\frac{\partial^2 \mathcal{C}_j(x,t)}{\partial x^2}}_{\text{diffusion}} = \underbrace{Z_j\left(\boldsymbol{\mathcal{C}}\left(x,t\right)\right)}_{\text{chemical reactions}}, \qquad x \in \left(0, L(t)\right). \tag{29}$$

The material derivative arises from differentiating Equation (12) with respect to time, and describes to the propagation of cell properties along cell boundary characteristics [6,7]. The term describing the effects of changes in cell length comes directly from the discrete mechanisms described in Equations (8)–(10). The linear diffusion term arises due to the choice of jump rates in Equations (4)–(7) of the discrete model [41]. Chemical reactions are described by $Z_j\left(\boldsymbol{\mathcal{C}}\left(x,t\right)\right)$, and originate from equivalent terms in the discrete model, $Z^{(j)}\left(\mathbf{C}_i\right)$.

Boundary conditions for $\mathcal{C}_j(x,t)$ are now formulated to ensure mass is conserved. As the left tissue boundary is fixed, we set $\partial \mathcal{C}_j/\partial x = 0$ at $x = 0$. At $x = L(t)$, we enforce that the total flux of $\mathcal{C}_j(x,t)$ in the frame of reference co-moving with the right tissue boundary is zero for all time,

$$\underbrace{u\left(L(t),t\right)\mathcal{C}_j\left(L(t),t\right) - D_j\frac{\partial \mathcal{C}_j\left(L(t),t\right)}{\partial x}}_{\text{total flux at } x = L(t)} - \underbrace{u\left(L(t),t\right)\mathcal{C}_j(L(t),t)}_{\text{moving frame of reference}} = 0, \tag{30}$$

where $u\left(L(t),t\right) = \mathrm{d}L/\mathrm{d}t$. Thus, $\partial \mathcal{C}_j/\partial x = 0$ at $x = L(t)$. Equation (29) can be written in

conservative form such that the free boundary mechanobiological model is:

$$\frac{\partial q(x,t)}{\partial t} = -\frac{1}{\eta}\frac{\partial^2 f(x,t)}{\partial x^2}, \qquad x \in (0, L(t)), \quad (31)$$

$$\frac{\partial \mathcal{C}_j(x,t)}{\partial t} + \frac{\partial}{\partial x}\left(u(x,t)\mathcal{C}_j(x,t) - D_j\frac{\partial \mathcal{C}_j(x,t)}{\partial x}\right) = Z_j(\boldsymbol{\mathcal{C}}(x,t)), \qquad x \in (0, L(t)), \quad (32)$$

$$0 = \frac{\partial f(x,t)}{\partial x}, \qquad x = 0, \quad (33)$$

$$0 = f(x,t) + \frac{1}{2q(x,t)}\frac{\partial f(x,t)}{\partial x} + \frac{1}{4q(x,t)}\left\{\frac{1}{q(x,t)}\frac{\partial a(\boldsymbol{\mathcal{C}}(x,t))}{\partial x}\frac{\partial k(\boldsymbol{\mathcal{C}}(x,t))}{\partial x}\right. \quad (34)$$
$$\left. + k(\boldsymbol{\mathcal{C}}(x,t))\frac{\partial}{\partial x}\left(\frac{1}{q(x,t)}\frac{\partial a(\boldsymbol{\mathcal{C}}(x,t))}{\partial x}\right) + a(\boldsymbol{\mathcal{C}}(x,t))\frac{\partial}{\partial x}\left(\frac{1}{q(x,t)}\frac{\partial k(\boldsymbol{\mathcal{C}}(x,t))}{\partial x}\right)\right\}, \qquad x = L(t),$$

$$u(x,t) = \frac{1}{\eta q(x,t)}\frac{\partial f(x,t)}{\partial x}, \qquad x \in (0, L(t)), \quad (35)$$

where

$$f(x,t) = k(\boldsymbol{\mathcal{C}})\left(\frac{1}{q(x,t)} - a(\boldsymbol{\mathcal{C}})\right), \qquad x \in (0, L(t)), \quad (36)$$

and $\partial \mathcal{C}_j/\partial x = 0$ at $x = 0$ and $x = L(t)$.

Equations (31)–(36) are solved numerically using a standard boundary fixing transformation [43]. In doing so, Equations (31)–(36) are transformed from an evolving domain, $0 \leq x \leq L(t)$, to a fixed domain, $0 \leq \xi \leq 1$, by setting $\xi = x/L(t)$ [43]. The transformed equations are discretised using a standard implicit finite difference method with initial conditions $q(x,0)$ and $\mathcal{C}_j(x,0)$. The numerical method is outlined in Appendix B.2 and key numerical algorithms are available on GitHub.

3 Results

To examine the accuracy of the new free boundary model, we compare solutions from the discrete and continuum models for epithelial tissues consisting of $m = 1$ and $m = 2$ chemical species.

3.1 Case study 1: Homogeneous tissue

In all simulations, an epithelial tissue with just $N = 20$ cells is considered. Choosing a relatively small value of N is a challenging scenario for the continuum model. Baker et al. [5] show that the accuracy of the continuum model increases as $N \to \infty$. Additional simulations with $N > 20$ confirm this (results not shown). In the discrete model, each cell i is initially the same length, $l_i(0) = 0.5$, such that $L(0) = 10$. The discrete cell density is $q_i(t) = 1/l_i(t)$ which corresponds to $q(x,0) = 2$ for $0 \leq x \leq L(0)$ in the continuum model.

The simplest application of the free boundary model is to consider cell populations without mechanobiological coupling. For a homogeneous tissue with one chemical species $\boldsymbol{\mathcal{C}}(x,t) = \mathcal{C}_1(x,t)$, the cell stiffness and cell resting length are constant and independent of $\mathcal{C}_1(x,t)$. Thus, the governing equations for $q(x,t)$ and $\mathcal{C}_1(x,t)$ are only coupled through the cell velocity, $u(x,t)$. To investigate how non-uniform tissue evolution affects the chemical concentration of cells, we set $\mathcal{C}_1(x,0) = 1$ for $0 \leq x \leq L(0)$ and $Z_1(\mathcal{C}_1) = 0$.

Figure 2(a) demonstrates a rapid decrease in the cell density at $x = L(t)$ as the tissue relaxes and the cells elongate. This decreases the chemical concentration (Figure 2(b)). As the tissue mechanically relaxes, the cell boundaries form a non-uniform spatial discretisation on which $\mathcal{C}_1(x,t)$

is transported (Figure 2(a)–(b)). Figure 2(c)–(d) compares discrete and continuum solutions, and demonstrates that the continuum model accurately reflects the biological mechanisms included in the discrete model. Additional results in Appendix C show that $q(x,t), \mathcal{C}_1(x,t)$ and $L(t)$ become constant as $t \to \infty$.

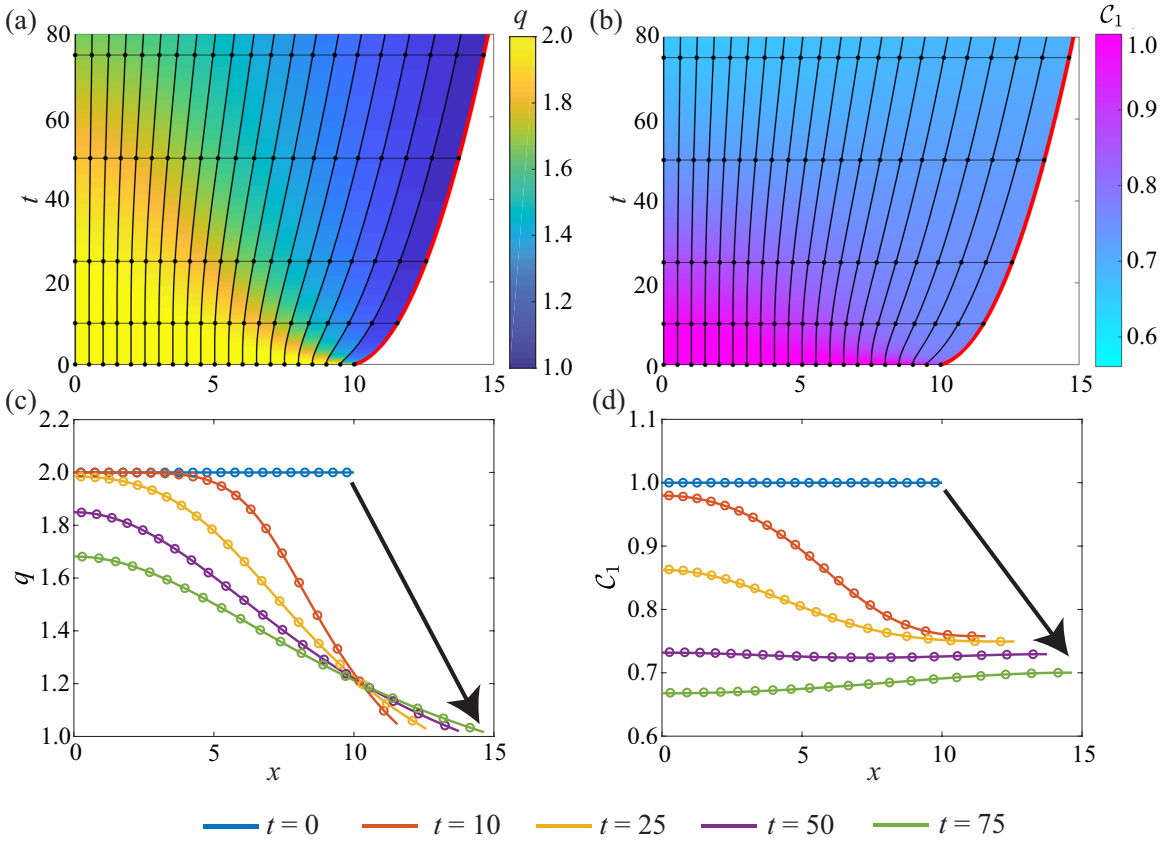

Figure 2: Homogeneous tissue with $N = 20$ cells and one chemical species where $Z_1(\mathcal{C}_1) = 0$, and $a = k = D_1 = \eta = 1$. Characteristic diagrams in (a)–(b) illustrate the position of cell boundaries where the free boundary is highlighted in red. The colour in (a)–(b) represents $q(x,t)$ and $\mathcal{C}_1(x,t)$ respectively. In (a)–(b), the black horizontal lines indicate times at which $q(x,t)$ and $\mathcal{C}_1(x,t)$ snapshots are shown in (c)–(d). In (c)–(d), the discrete and continuum solutions are compared as the dots and solid line respectively for $t = 0, 10, 25, 50, 75$ where the arrow represents the direction of time.

3.2 Case study 2: Rac–Rho pathway

We now apply the mechanobiological model to investigate the Rac–Rho pathway. Rho GTPases are a family of signalling molecules that consist of two key members, RhoA and Rac1. Rho GTPases cycle between an active and inactive state, and regulate cell size and cell motility [12, 35, 37, 44, 45]. Additionally, Rho GTPases play roles in wound healing [46] and cancer development [47, 48]. New experimental methods [49, 50] have discovered a connection between cellular mechanical tension and Rho GTPase activity [51]. Previous studies use a discrete modelling framework to investigate this relationship, and conclude that epithelial tissue dynamics is dictated by the strength of the mechanobiological coupling [12,33]. We extend these previous results by considering how mechanobiological coupling, and chemical variation associated with changes in cell length and diffusion, lead to oscillatory and non-oscillatory tissue dynamics.

To investigate the impact of mechanobiological coupling on epithelial tissue dynamics, we let $\boldsymbol{\mathcal{C}}(x,t) = \{\mathcal{C}_1(x,t), \mathcal{C}_2(x,t)\}$ such that $\mathcal{C}_1(x,t)$ is the concentration of RhoA and $\mathcal{C}_2(x,t)$ is the concentration of Rac1. In the discrete and continuum models, cells are assumed to behave like linear springs [8, 9]. Thus, cellular mechanical tension is defined as the difference between the length and resting length of cells. Mechanobiological coupling is proportional to cellular tension and is included in $Z_j\left(\boldsymbol{\mathcal{C}}\right)$. As Rho GTPase activity increases cell stiffness [52], we choose $k\left(\boldsymbol{\mathcal{C}}\right)$ as an increasing function of either $\mathcal{C}_1(x,t)$ or $\mathcal{C}_2(x,t)$. Furthermore, $a\left(\boldsymbol{\mathcal{C}}\right)$ is chosen to reflect the fact that RhoA promotes cell contraction [12, 33].

The effect of RhoA, $\mathcal{C}_1(x,t)$, on epithelial tissue dynamics is considered first. We include the same mechanobiological coupling as [12, 33] and let,

$$Z_1\left(\mathcal{C}_1\right) = \overbrace{\left(b + \underbrace{\gamma \frac{\mathcal{C}_1^n}{1+\mathcal{C}_1^n}}_{\text{feedback loop}} + \underbrace{\beta\left(\frac{1}{q} - a\left(\mathcal{C}_1\right)\right)}_{\substack{\text{mechanobiological} \\ \text{coupling}}}\right)\left(G_{\mathrm{T}} - \mathcal{C}_1\right)}^{\text{activation}} \underbrace{- \delta \mathcal{C}_1}_{\text{deactivation}}, \tag{37}$$

where b is the basal activation rate, G_{T} is the total amount of active and inactive RhoA, and δ is the deactivation rate [12,33]. The activation term contains a positive feedback loop, governed by γ, to reflect the fact that RhoA self–activates [12, 33]. Mechanobiological coupling is governed by β, and is proportional to mechanical tension.

Similar to [12], we find that the tissue either mechanically relaxes or continuously oscillates depending on the choice of β (Figure 3). Figure 3(a),(c) illustrates non-oscillatory tissue behaviour when the mechanobiological coupling is weak, $\beta = 0.2$. By increasing the strength of the mechanobiological coupling to $\beta = 0.3$, we observe temporal oscillations in the tissue length and sharp transitions between high and low levels of RhoA (Figure 3(b),(d)). Figure 3(e)–(h) illustrates that the continuum model and the free boundary condition accurately describe non-oscillatory and oscillatory tissue dynamics.

As diffusion is usually considered a stabilising process [53], we hypothesise that increasing D_1 will smooth the oscillations that arise when $\beta = 0.3$. Figure 4 illustrates that as D_1 increases, the amplitude of the oscillations remains constant, but the timing is delayed. While this delay is not significant for a weakly coupled system (Figure 4(a)), it is significant for a strongly coupled system (Figure 4(b)). Thus, diffusion does not significantly dampen the oscillations. This test case provides further evidence of the ability of the new continuum model and free boundary condition to capture key biological mechanisms included in the discrete model (Figure 4).

To examine the combined effect of RhoA and Rac1 on epithelial tissue dynamics, we let [12],

$$Z_1(\boldsymbol{\mathcal{C}}) = \overbrace{\left(b_1 + \hat{\beta}\underbrace{\left(\frac{1}{q} - a(\mathcal{C}_1)\right)}_{\substack{\text{mechanobiological}\\ \text{coupling}}}\right)\frac{1}{1+\mathcal{C}_2^n}(G_{1_T} - \mathcal{C}_1)}^{\text{activation}} - \underbrace{\delta_1 \mathcal{C}_1}_{\text{deactivation}}, \tag{38}$$

$$Z_2(\boldsymbol{\mathcal{C}}) = \underbrace{\frac{b_2}{1+\mathcal{C}_1^n}(G_{2_T} - \mathcal{C}_2)}_{\text{activation}} - \underbrace{\delta_2 \mathcal{C}_2}_{\text{deactivation}}. \tag{39}$$

In a weakly coupled system when $\hat{\beta} = 1$, we observe the fast transition from the initial concentrations of RhoA and Rac1 to the steady state concentration (Figure 5(a),(c)). Analogous to Figure 3(a),(c), temporal oscillations arise when the mechanobiological coupling is strong, $\hat{\beta} = 2.5$ (Figure 5(b),(d)).

The mechanobiological coupling and intracellular signalling in Figures 3–5 extend upon previous Rho GTPase models [12, 33]. The source terms stated in Equations (37)–(39) can be applied to a single, spatially–uniform cell to determine the dependence of the system stability on model parameters [12]. This analysis is outlined in Appendix D.1 and was used to inform our choices of β and $\hat{\beta}$.

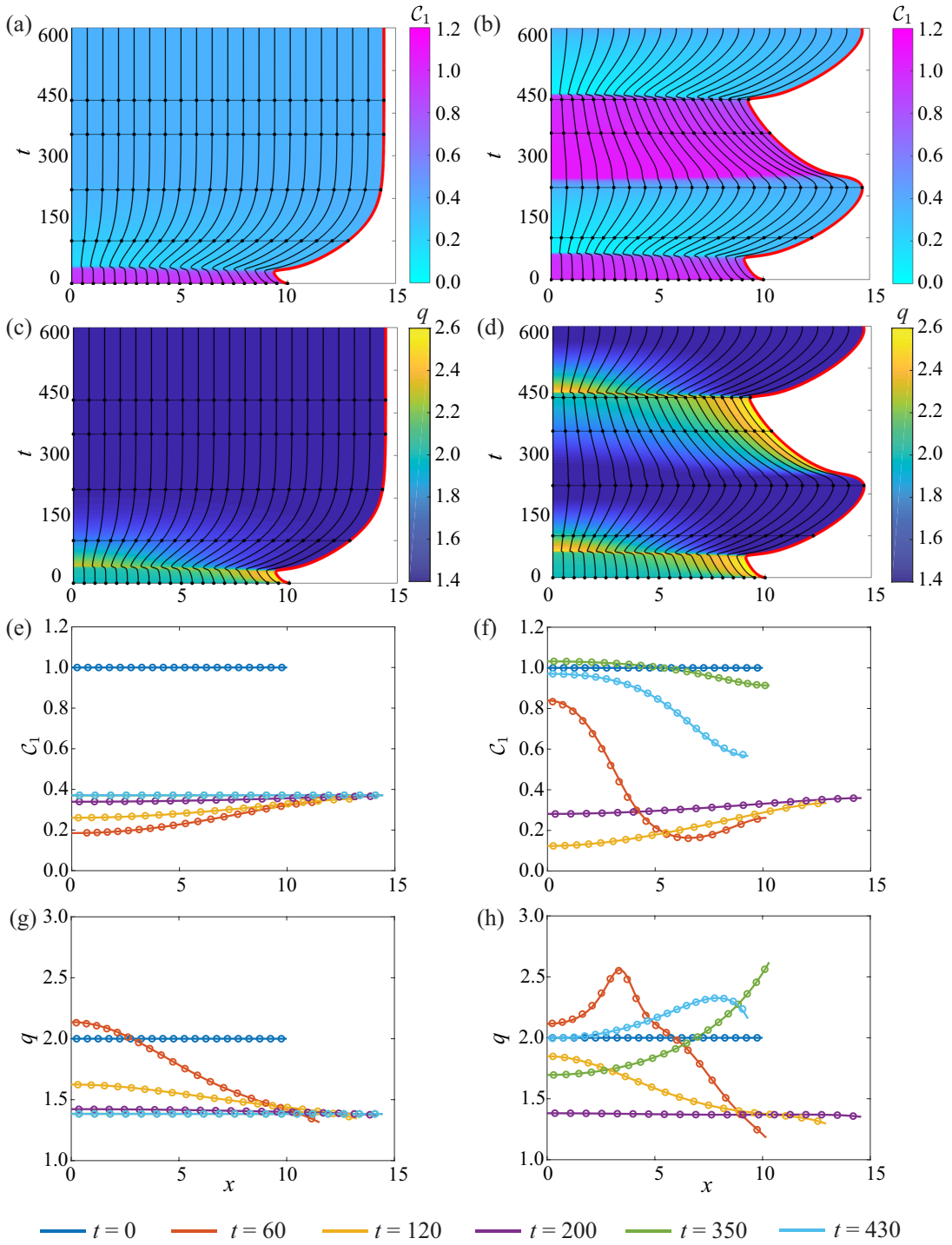

Figure 3: 1D tissue dynamics where RhoA is coupled to mechanical cell tension. (a),(c),(e),(g) correspond to a non-oscillatory system where $\beta = 0.2$ and (b),(d),(f),(h) relate to an oscillatory system where $\beta = 0.3$. Characteristic diagrams in (a)–(d) illustrate the evolution of cell boundaries where the free boundary is highlighted in red. The colour in (a)–(b) represents $\mathcal{C}_1(x,t)$ and $q(x,t)$ in (c)–(d). The black horizontal lines indicate times at which $\mathcal{C}_1(x,t)$ and $q(x,t)$ snapshots are shown in (e)–(f) and (g)–(h) respectively. In (e)–(h), the discrete and continuum solutions are compared as the dots and solid line respectively for $t = 0, 100, 220, 350, 430$. In both systems, $a = l_0 - \phi \mathcal{C}_1^p / \left(G_\mathrm{h}^p + \mathcal{C}_1^p\right)$, $k = 1 + 0.05\mathcal{C}_1$, $D_1 = 1$, $\eta = 1$, and $\mathcal{C}_1(0,t) = 1$ for $0 \leq x \leq L(0)$. Parameters: $b = 0.2$, $\gamma = 1.5$, $n = 4$, $p = 4$, $G_\mathrm{T} = 2$, $l_0 = 1$, $\phi = 0.65$, $G_\mathrm{h} = 0.4$, $\delta = 1$.

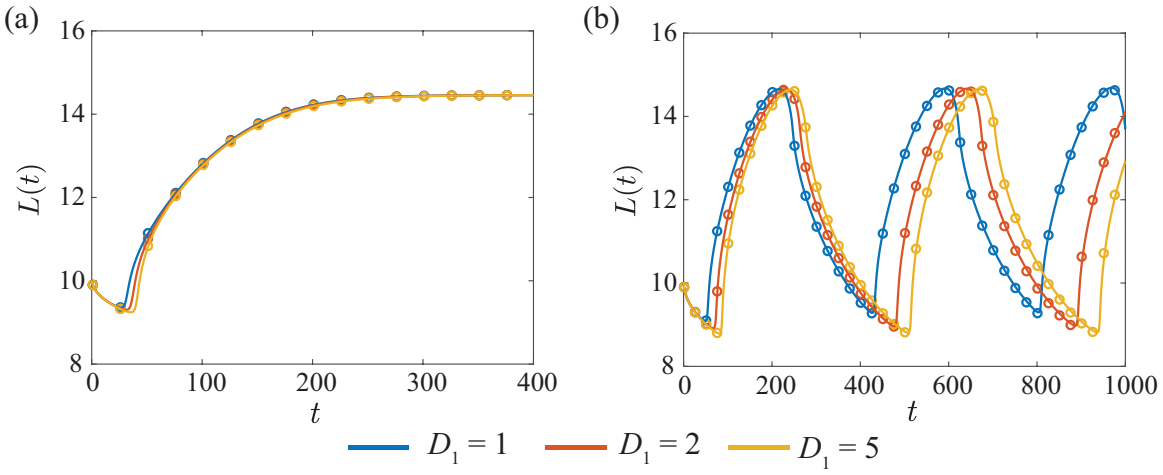

Figure 4: The effect of diffusion on the dynamics of the free boundary for (a) a non-oscillatory system with $\beta = 0.2$ and (b) a oscillatory system with $\beta = 0.3$. The discrete solution is shown as the dots and the continuum solution as solid line. Parameters are as in Figure 3.

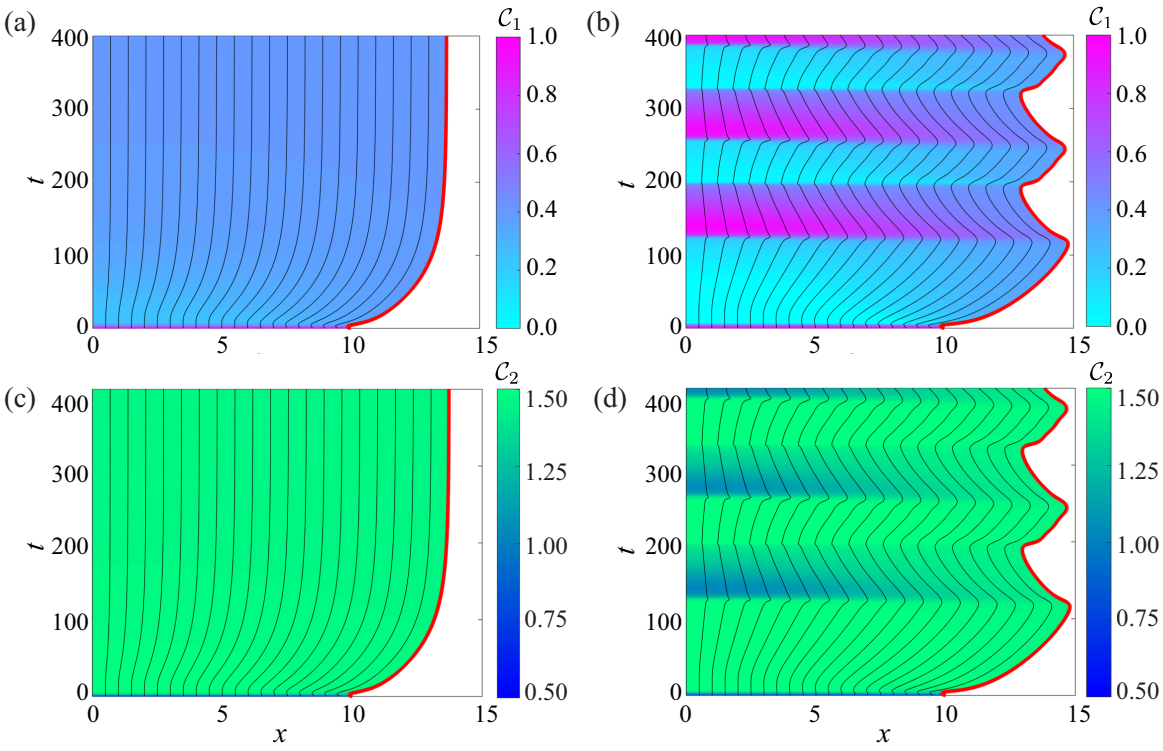

Figure 5: Characteristic diagrams for the interaction of RhoA and Rac1 where the free boundary is highlighted in red. (a),(c) correspond to a non-oscillatory system where $\hat{\beta} = 1$ and (b),(d) relate to an oscillatory system where $\hat{\beta} = 2.5$. The colour in (a)–(b) denotes the concentration of RhoA and the concentration of Rac1 in (c)–(d). In both systems, $a = l_0 - \phi \mathcal{C}_1^p / \left(G_{\mathrm{h}}^p + \mathcal{C}_1^p\right)$, $k = 1 + 0.1\mathcal{C}_2$, $D_1 = D_2 = 1$ and $\eta = 1$. The initial conditions are $\mathcal{C}_1(0,t) = 1$ and $\mathcal{C}_2(0,t) = 0.5$ for $0 \leq x \leq L(0)$. Parameters: $b_1 = b_2 = 1$, $\delta_1 = \delta_2 = 1$, $n = 3$, $p = 4$, $G_{1_{\mathrm{T}}} = 2$, $G_{2_{\mathrm{T}}} = 3$, $l_0 = 1$, $\phi = 0.65$, $G_{\mathrm{h}} = 0.4$. Discrete and continuum solutions are compared in Appendix D.

3.3 Case study 3: Activator–inhibitor patterning

Case study 3 considers an activator–inhibitor system [53–55]. Previous studies of activator–inhibitor patterns on uniformly evolving domains have characterised the pattern splitting and frequency doubling phenomena which occur naturally on the skin of angelfish [25–28, 56]. To investigate how diffusion driven instabilities arise on a non-uniformly evolving domain, we let $\boldsymbol{\mathcal{C}}(x,t) = \{\mathcal{C}_1(x,t), \mathcal{C}_2(x,t)\}$ with $D_1 \neq D_2$, and use Schnakenberg kinetics,

$$Z_1\left(\boldsymbol{\mathcal{C}}\right) = n_1 - n_2\mathcal{C}_1 + n_3\mathcal{C}_1^2\mathcal{C}_2, \tag{40}$$

$$Z_2\left(\boldsymbol{\mathcal{C}}\right) = n_4 - n_3\mathcal{C}_1^2\mathcal{C}_2, \tag{41}$$

where $\mathcal{C}_1(x,t)$ is the activator and $\mathcal{C}_2(x,t)$ is the inhibitor [53]. The parameters, $n_i > 0$ for $i = 1, 2, 3, 4$, govern activator–inhibitor interactions. Non-dimensionalisation of the governing equations (Equations (25) and (29)) reveals that the linear stability analysis is analogous to the classical stability analysis of Turing patterns on fixed domains [53]. Thus, we define the relative diffusivity, $d = D_2/D_1$, with the expectation that there exists a critical value, d_c, that depends upon the choice of n_i. In doing so, it is expected that diffusion driven instabilities arise for $d > d_c$ [53, 54].

A homogeneous tissue is initialised to investigate the affect of d on the evolution of activator–inhibitor patterns. For $d < d_c$, the distribution of $\mathcal{C}_1(x,t)$ and $\mathcal{C}_2(x,t)$ varies in time but remains approximately spatially uniform throughout the tissue (Figure 6(a),(c),(e),(g)). Thus, only temporal patterning arises when $d < d_c$. Figure 6(b),(d),(f),(h) demonstrates that spatial–temporal patterns develop when $d > d_c$. Similar to [25–27], we observe splitting in activator peaks for $d > d_c$ where the concentration of $\mathcal{C}_1(x,t)$ is at a minimum. Figure 6(b) shows that two distinct activator peaks arise. The long time behaviour of the tissue is examined in Appendix E. Figure 6(e),(g) shows excellent agreement between the solutions of the discrete and continuum models when $d < d_c$, whereas Figure 6(f),(h) shows a small discrepancy between the solutions of the discrete and continuum models when $d > d_c$.

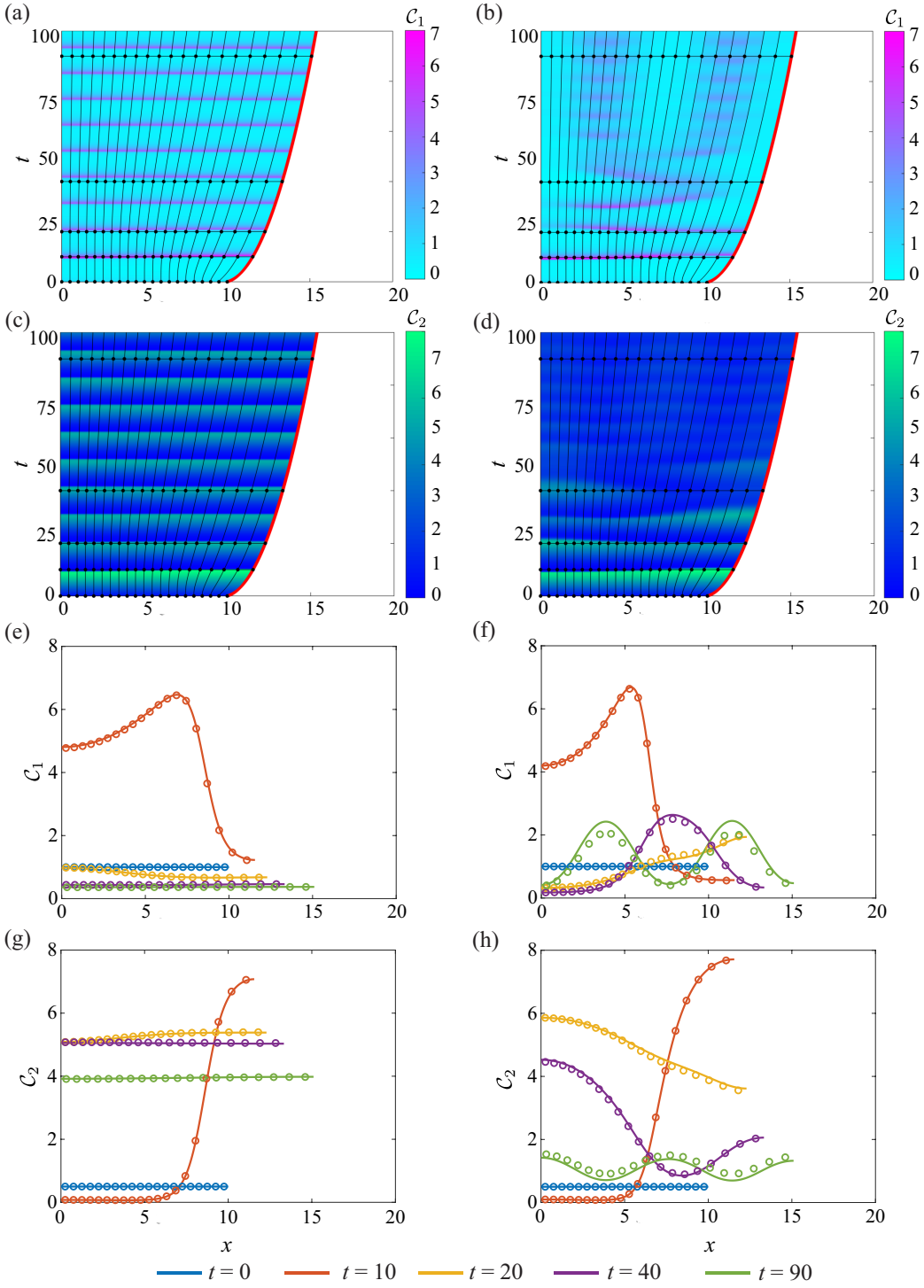

Figure 6: The evolution of activator–inhibitor patterns in a homogeneous tissue with Schnakenberg dynamics. In (a),(c),(e),(g), $D_1 = 2$ and $D_2 = 3$ such that $d < d_c$. In (b),(d),(f),(h), $D_1 = 0.5$ and $D_2 = 5$ such that $d > d_c$. Characteristic diagrams in (a)–(d) illustrate the evolution of cell boundaries where the free boundary is highlighted in red. The colour in (a)–(b) represents $\mathcal{C}_1(x,t)$ and $\mathcal{C}_2(x,t)$ in (c)–(d). The black horizontal lines indicate times at which $\mathcal{C}_1(x,t)$ and $\mathcal{C}_2(x,t)$ snapshots are shown in (e)–(f) and (g)–(h) respectively. In (e)–(h), the discrete and continuum solutions are compared as the dots and solid line respectively for $t = 0, 10, 20, 40, 90$. In both systems, $\mathcal{C}_1(x,0) = 1$ and $\mathcal{C}_2(x,0) = 0.5$ for $0 \leq x \leq L(0)$ and $a = k = \eta = 1$ Parameters: $n_1 = 0.1, n_2 = 1, n_3 = 0.5, n_4 = 1$ and $d_c = 4.9842$

4 Conclusion

In this study, we present a novel free boundary mechanobiological model to describe epithelial tissue dynamics. A discrete modelling framework is used to include mechanobiological coupling at the cell level. Tissue–level outcomes are described by a system of coupled, non-linear partial differential equations. In contrast to previous free boundary models [22–28], the free boundary condition is not pre-specified to correspond to uniformly evolving tissues, or a one–phase Stefan condition [20,21]. We take the continuum limit description of the discrete model to derive a new free boundary condition which describes how mechanobiological coupling dictates epithelial tissue dynamics. In deriving the continuum model, we make reasonable assumptions about the number of cells and the rate of mechanical relaxation. Case studies involving a homogeneous cell population, the Rac–Rho pathway and activator–inhibitor patterning demonstrate that the continuum model reflects the biologically–motivated discrete model even when N is relatively small. In addition, these case studies show how non-uniform tissue dynamics, including oscillatory and non-oscillatory tissue behaviour, arises due to mechanobiological coupling.

The accuracy of the continuum model increases as $N \to \infty$ [5]. One potential approach to improve the accuracy of the continuum model is to retain additional terms in the truncated Taylor series used to derive the continuum model. We do not follow this approach for two reasons. First, retaining higher order terms can lead to ill–posed partial differential equation models [57]. Second, numerical exploration has confirmed that solutions of the discrete and continuum models agree for a relatively small value of $N = 20$. Therefore, we leave the question of retaining additional terms in the truncated Taylor series for future consideration.

There are several possible mathematical and biological extensions of this study. We take the most fundamental approach and choose a linear force law to describe cell-to-cell interactions. One extension of this work is to describe cell-to-cell interactions using a non-linear force law [5, 9]. Another choice we make is to suppose that chemical transport is described by linear diffusion at the macroscopic scale. Other choices, such as diffusion with drift, are also possible [58]. An important extension of the free boundary model is to introduce cell proliferation and cell death [5, 7, 59]. While these phenomena traditionally depend on cell length [5, 7], the general theoretical framework presented here is compatible with cell proliferation and death that depend on intracellular signalling. In doing so, the model is applicable to biochemical networks where biological mechanisms regulate cell proliferation in epithelial tissues [60].

Data access: MATLAB implementations of key numerical algorithms is available on GitHub.

Author Contributions: All authors contributed equally to the design of the study. TAT performed numerical simulations with the assistance of RJM. TAT drafted the article and all authors gave approval for publication.

Competing interests: The authors declare they have no competing interests.

Acknowledgements: This work is supported by the Australian Research Council (DP200100177, DP180101797). We acknowledge the computational resources provided by the High Performance Computing and Research Support Group.

Appendices

A Continuum model derivation

A.1 Change of variables

This section outlines the change of variables from $(\bar{i}, t)$ to (x, t) used in Section 2.2. Rewriting Equation (11), the cell density per unit length, $q(x,t)$, is

$$q(x,t) = N\frac{\partial \bar{i}(x,t)}{\partial x}. \tag{42}$$

To perform a change of variables from $(\bar{i}, t)$ to (x, t), we calculate the Jacobian of the coordinate transformation [5, 8, 9],

$$\begin{pmatrix} \frac{\partial x}{\partial \bar{i}}\big|_t & \frac{\partial x}{\partial t}\big|_{\bar{i}} \\ \frac{\partial t}{\partial \bar{i}}\big|_t & \frac{\partial t}{\partial t}\big|_{\bar{i}} \end{pmatrix} = \begin{pmatrix} \frac{\partial \bar{i}}{\partial x}\big|_t & \frac{\partial \bar{i}}{\partial t}\big|_x \\ \frac{\partial t}{\partial x}\big|_t & \frac{\partial t}{\partial t}\big|_x \end{pmatrix}^{-1}, \tag{43}$$

$$= \frac{1}{\frac{\partial \bar{i}}{\partial x}\big|_t \frac{\partial t}{\partial t}\big|_x - \frac{\partial \bar{i}}{\partial t}\big|_x \frac{\partial t}{\partial x}\big|_t} \begin{pmatrix} \frac{\partial t}{\partial t}\big|_x & -\frac{\partial \bar{i}}{\partial t}\big|_x \\ -\frac{\partial t}{\partial x}\big|_t & \frac{\partial \bar{i}}{\partial x}\big|_t \end{pmatrix}, \tag{44}$$

to arrive at the relationships,

$$\frac{\partial x}{\partial \bar{i}} = \frac{N}{q}, \qquad \frac{\partial x}{\partial t} = -\frac{N}{q}\frac{\partial \bar{i}}{\partial t}. \tag{45}$$

Using the chain rule, the second derivatives are,

$$\frac{\partial^2 x}{\partial \bar{i}^2} = \frac{\partial x}{\partial \bar{i}}\frac{\partial}{\partial x}\left(\frac{N}{q}\right) = -\frac{N^2}{q^3}\frac{\partial q}{\partial x}, \tag{46}$$

$$\frac{\partial^2 k}{\partial \bar{i}^2} = \frac{\partial x}{\partial \bar{i}}\frac{\partial}{\partial x}\left(\frac{\partial k}{\partial x}\frac{\partial x}{\partial \bar{i}}\right) = \frac{N^2}{q}\frac{\partial}{\partial x}\left(\frac{1}{q}\frac{\partial k}{\partial x}\right), \tag{47}$$

$$\frac{\partial^2 a}{\partial \bar{i}^2} = \frac{\partial x}{\partial \bar{i}}\frac{\partial}{\partial x}\left(\frac{\partial a}{\partial x}\frac{\partial x}{\partial \bar{i}}\right) = \frac{N^2}{q}\frac{\partial}{\partial x}\left(\frac{1}{q}\frac{\partial a}{\partial x}\right). \tag{48}$$

A.2 Derivation of governing equation for cell density in factorised form

Here we outline how Equations (23), (25) and (28) can be obtained using the factorised form of $f(\bar{i}, t)$ in Equation (13). The equations of motion in Equations (14)–(16) are restated as,

$$\eta\frac{\partial x(\bar{i},t)}{\partial t} = 0, \qquad \bar{i} = 0, \tag{49}$$

$$\eta\frac{\partial x(\bar{i},t)}{\partial t} = f(\bar{i} + 1/N, t) - f(\bar{i}, t), \qquad \bar{i} \in (1/N, 1), \tag{50}$$

$$\eta\frac{\partial x(\bar{i},t)}{\partial t} = -f(\bar{i}, t), \qquad \bar{i} = 1. \tag{51}$$

To derive the local cell velocity in Equation (23), the right hand side of Equation (50) is expanded in a Taylor series about $\bar{i}$,

$$\eta\frac{\partial x}{\partial t} = \frac{1}{N}\frac{\partial f}{\partial \bar{i}} + \mathcal{O}\left(N^{-2}\right), \qquad \bar{i} \in (1/N, 1). \tag{52}$$

Neglecting non-zero higher order terms and using the chain rule gives,

$$\eta \frac{\partial x}{\partial t} = \frac{1}{N} \frac{\partial f}{\partial x} \frac{\partial x}{\partial \bar{i}}, \qquad \bar{i} \in (1/N, 1). \tag{53}$$

Equation (45) is substituted into the right hand side of Equation (53) to derive the local cell velocity, $u(x,t) = \partial x/\partial t$, as,

$$u(x,t) = \frac{1}{\eta q(x,t)} \frac{\partial f(x,t)}{\partial x}, \qquad x \in (0, L(t)). \tag{54}$$

As $u(x,t) = \partial x/\partial t$, Equation (45) is substituted into the left hand side of Equation (54). Differentiating the resulting equation with respect to x gives,

$$\frac{\partial}{\partial x}\left(N \frac{\partial \bar{i}}{\partial t}\right) = \frac{\partial}{\partial x}\left(-\frac{1}{\eta} \frac{\partial f(x,t)}{\partial x}\right), \qquad x \in (0, L(t)). \tag{55}$$

The order of differentiation on the left hand side of Equation (55) is reversed, and Equation (45) is used to give,

$$\frac{\partial q(x,t)}{\partial t} = -\frac{1}{\eta} \frac{\partial^2 f(x,t)}{\partial x^2}, \qquad x \in (0, L(t)). \tag{56}$$

To derive the left boundary condition in Equation (28), the left hand side of Equation (49) is equated to Equation (54) giving,

$$\frac{\partial f(x,t)}{\partial x} = 0, \qquad x = 0. \tag{57}$$

Thus, we have shown that Equations (23), (25) and (28) can be obtained using the factorised form of $f(\bar{i}, t)$ in Equation (13) and first order Taylor series expansions. In the main document we do not peruse this approach. This is because more care is required to obtain the correct form of the free boundary equation in Equation (27). Extensive numerical exploration confirms that the approach taken in the main document is necessary to reflect the underlying biological mechanisms included in the discrete model.

B Numerical methods

This section outlines the numerical method used to solve the discrete and continuum models with one chemical species, $m = 1$. Key numerical algorithms for $m = 1$ and $m = 2$ chemical species are available on GitHub.

B.1 Discrete model

For N cells and one chemical species, the discrete model consists of $2N + 1$ ordinary differential equations. For simplicity, we write $\mathbf{C} = C^{(1)} = C$ and $D_1 = D$. Equations (1)–(10) are restated as:

$$\eta \frac{\mathrm{d}x_0}{\mathrm{d}t} = 0, \tag{58}$$

$$\eta \frac{\mathrm{d}x_i}{\mathrm{d}t} = f_{i+1} - f_i, \qquad i = 1, \ldots, N-1, \tag{59}$$

$$\eta \frac{\mathrm{d}x_N}{\mathrm{d}t} = -f_N, \tag{60}$$

$$\frac{\mathrm{d}C_1}{\mathrm{d}t} = Z\left(C_1\right) - \frac{C_1}{l_1}\frac{\mathrm{d}l_1}{\mathrm{d}t} + \frac{1}{l_1}\left(T_2^- C_2 l_2 - T_1^+ C_1 l_1\right), \tag{61}$$

$$\begin{aligned}\frac{\mathrm{d}C_i}{\mathrm{d}t} &= Z\left(C_i\right) - \frac{C_i}{l_i}\frac{\mathrm{d}l_i}{\mathrm{d}t} \\ &+ \frac{1}{l_i}\left(T_{i-1}^+ C_{i-1} l_{i-1} - \left(T_i^+ + T_i^-\right) C_i l_i + T_{i+1}^- C_{i+1} l_{i+1}\right), \qquad i = 1, \ldots, N-1,\end{aligned} \tag{62}$$

$$\frac{\mathrm{d}C_N}{\mathrm{d}t} = Z\left(C_N\right) - \frac{C_N}{l_N}\frac{\mathrm{d}l_N}{\mathrm{d}t} + \frac{1}{l_N}\left(T_{N-1}^+ C_{N-1} l_{N-1} - T_N^- C_N l_N\right), \tag{63}$$

where $l_i = x_i(t) - x_{i-1}(t)$ is the length of cell i and

$$f_i = k\left(C_i\right)\left(x_i(t) - x_{i-1}(t) - a\left(C_i\right)\right), \qquad i = 1, \ldots, N. \tag{64}$$

The transport rates for internal cells are

$$T_i^- = \frac{2D}{\left(y_i(t) - y_{i-1}(t)\right)\left(y_{i+1}(t) - y_{i-1}(t)\right)}, \qquad i = 2, \ldots, N-1, \tag{65}$$

$$T_i^+ = \frac{2D}{\left(y_{i+1}(t) - y_i(t)\right)\left(y_{i+1}(t) - y_{i-1}(t)\right)}, \qquad i = 2, \ldots, N-1, \tag{66}$$

and

$$T_1^+ = \frac{2D}{\left(y_2(t) - y_1(t)\right)\left(y_2(t) + y_1(t)\right)}, \tag{67}$$

$$T_N^- = \frac{2D}{\left(y_N(t) - y_{N-1}(t)\right)\left(x_N(t) - y_N(t) - y_{N-1}(t)\right)}, \tag{68}$$

for boundary cells [41]. Equations (58)–(68) are solved numerically using `ode15s` in MATLAB [42]. At each time step, we use a Voronoi partition to compute the resident points, $y_i(t)$, and the transport rates, $T_i^{\pm}$.

B.1.1 Voronoi partition

To define a Voronoi partition, we set the resident point of cell 1, $y_1(t)$, as the midpoint of its respective cell boundaries,

$$y_1(t) = \frac{x_0(t) + x_1(t)}{2}. \tag{69}$$

The Voronoi partition enforces that the cell boundaries correspond to the midpoints of resident points [41]. Thus, the following relationship holds

$$x_{i-1}(t) = \frac{y_i(t) + y_{i-1}(t)}{2}, \qquad i = 2, \ldots, N. \tag{70}$$

Equations (69) and (70) can be written as the following system of linear equations,

$$\begin{bmatrix} 1 & 0 & 0 & 0 & 0 \\ 1 & 1 & 0 & 0 & 0 \\ 0 & 1 & 1 & 0 & 0 \\ \vdots & \ddots & \ddots & \ddots & \ddots \\ 0 & 0 & 0 & 1 & 1 \end{bmatrix} \begin{bmatrix} y_1(t) \\ y_2(t) \\ y_3(t) \\ \vdots \\ y_N(t) \end{bmatrix} = \begin{bmatrix} (x_0(t) + x_1(t))/2 \\ 2x_1(t) \\ 2x_2(t) \\ \vdots \\ 2x_{N-1}(t) \end{bmatrix}. \tag{71}$$

Equation (71) is solved numerically for the resident points at each time step of the discrete simulation. As Equation (71) is a lower triangular matrix system, we use the Thomas Algorithm [61].

B.2 Continuum model

We now outline the numerical method used to solve the continuum model and write $\boldsymbol{\mathcal{C}} = \mathcal{C}_1 = \mathcal{C}$ and $D_1 = D$ for simplicity. Equations (31)–(36) are restated as a system of coupled, non-linear partial differential equations:

$$\frac{\partial q}{\partial t} = -\frac{1}{\eta}\frac{\partial^2 f}{\partial x^2}, \qquad x \in (0, L(t)), \tag{72}$$

$$\frac{\partial \mathcal{C}}{\partial t} + \frac{\partial}{\partial x}\left(u\mathcal{C} - D\frac{\partial \mathcal{C}}{\partial x}\right) = Z(\mathcal{C}), \qquad x \in (0, L(t)), \tag{73}$$

$$0 = \frac{\partial f}{\partial x}, \qquad x = 0, \tag{74}$$

$$0 = f + \frac{1}{2q}\frac{\partial f}{\partial x} + \frac{1}{4q}\left\{\frac{1}{q}\frac{\partial a}{\partial x}\frac{\partial k}{\partial x} + k\frac{\partial}{\partial x}\left(\frac{1}{q}\frac{\partial a}{\partial x}\right) + a\frac{\partial}{\partial x}\left(\frac{1}{q}\frac{\partial k}{\partial x}\right)\right\}, \qquad x = L(t), \tag{75}$$

$$u = \frac{1}{\eta q}\frac{\partial f}{\partial x}, \qquad x \in (0, L(t)), \tag{76}$$

where

$$f = k\left(\frac{1}{q} - a\right), \qquad x \in (0, L(t)), \tag{77}$$

and $\partial \mathcal{C}/\partial x = 0$ at $x = 0$ and $x = L(t)$.

A standard boundary fixing transformation is used to transform Equations (72)–(77) from an evolving domain, $0 \leq x \leq L(t)$, to a fixed domain, $0 \leq \xi \leq 1$, by setting $\xi = x/L(t)$ [43]. Invoking

this transform yields:

$$\frac{\partial q}{\partial t} = -\frac{1}{\eta L^2}\frac{\partial^2 f}{\partial \xi^2} + \frac{\xi}{L}\frac{\mathrm{d}L}{\mathrm{d}t}\frac{\partial q}{\partial \xi}, \qquad \xi \in (0,1), \tag{78}$$

$$\frac{\partial \mathcal{C}}{\partial t} + v\frac{\partial \mathcal{C}}{\partial \xi} + \frac{\mathcal{C}}{\eta q L^2}\left\{\frac{\partial^2 f}{\partial \xi^2} - \frac{1}{q}\frac{\partial q}{\partial \xi}\frac{\partial f}{\partial \xi}\right\} - \frac{D}{L^2}\frac{\partial^2 \mathcal{C}}{\partial \xi^2} = Z(\mathcal{C}), \qquad \xi \in (0,1), \tag{79}$$

$$0 = \frac{1}{L}\frac{\partial f}{\partial \xi}, \qquad \xi = 0, \tag{80}$$

$$0 = f + \frac{1}{2qL}\frac{\partial f}{\partial \xi} + \frac{k}{4qL^2}\frac{\partial}{\partial \xi}\left(\frac{1}{q}\frac{\partial a}{\partial \xi}\right) + \frac{1}{4q^2L^2}\frac{\partial a}{\partial \xi}\frac{\partial k}{\partial \xi} + \frac{a}{4qL^2}\frac{\partial}{\partial \xi}\left(\frac{1}{q}\frac{\partial k}{\partial \xi}\right), \qquad \xi = 1, \tag{81}$$

$$u = \frac{1}{\eta q L}\frac{\partial f}{\partial \xi}, \qquad \xi \in (0,1), \tag{82}$$

where

$$v = \frac{1}{\eta q L^2}\frac{\partial f}{\partial \xi} - \frac{\xi}{L}\frac{\mathrm{d}L}{\mathrm{d}t}, \qquad \xi \in (0,1), \tag{83}$$

and $\partial \mathcal{C}/\partial \xi = 0$ at $\xi = 0$ and $\xi = 1$.

Equations (78)–(83) are spatially discretised on a uniform mesh, with $n = 1/\Delta\xi + 1$ nodes. The value of $q(\xi, t)$ and $\mathcal{C}(\xi, t)$ at the i^{th} spatial node and the j^{th} temporal node are approximated as q_i^j and $\mathcal{C}_i^j$ respectively, where $\xi = (i-1)\Delta\xi$ and $t = j\Delta t$. A standard implicit finite difference method is used to approximate spatial and temporal derivatives [61].

We first consider the discretisation of the governing equation and boundary conditions for cell density. Central difference approximations are used to discretise Equation (78) as

$$\begin{aligned}\frac{q_i^{j+1} - q_i^j}{\Delta t} = &-\frac{1}{\eta (L^{j+1})^2}\left(\frac{f_{i-1}^{j+1} - 2f_i^{j+1} + f_{i+1}^{j+1}}{(\Delta\xi)^2}\right) \\ &+ \frac{\xi}{L^{j+1}}\left(\frac{L^{j+1} - L^j}{\Delta t}\right)\left(\frac{q_{i+1}^{j+1} - q_{i-1}^{j+1}}{2\Delta\xi}\right), \qquad i = 2, \ldots, n-1.\end{aligned} \tag{84}$$

Equations (80) and (81) are discretised using appropriate forward and backward difference approximations,

$$0 = f_2^{j+1} - f_1^{j+1}, \tag{85}$$

$$\begin{aligned}0 = &f_n^{j+1} + \frac{1}{2q_n^{j+1}L^{j+1}}\left(\frac{f_n^{j+1} - f_{n-1}^{j+1}}{\Delta\xi}\right) + \frac{k_n^{j+1}}{4q_n^{j+1}(L^{j+1})^2}\left(\frac{1}{q_n^{j+1}} - \frac{1}{q_{n-1}^{j+1}}\right)\left(\frac{a_n^{j+1} - a_{n-1}^{j+1}}{\Delta\xi}\right) \\ &+ \frac{a_n^{j+1}}{4q_n^{j+1}(L^{j+1})^2}\left(\frac{1}{q_n^{j+1}} - \frac{1}{q_{n-1}^{j+1}}\right)\left(\frac{k_n^{j+1} - k_{n-1}^{j+1}}{\Delta\xi}\right) \\ &+ \frac{1}{4\left(q_i^{j+1}\right)^2(L^{j+1})^2}\left(\frac{a_n^{j+1} - a_{n-1}^{j+1}}{\Delta\xi}\right)\left(\frac{k_n^{j+1} - k_{n-1}^{j+1}}{\Delta\xi}\right).\end{aligned} \tag{86}$$

We now consider the discretisation of the governing equation and boundary conditions for $\mathcal{C}$. As $\mathcal{C}$ propagates along cell boundary characteristics, Equation (83) is used to upwind the first derivative of $\mathcal{C}$ in Equation (79). For $v_i > 0$, a backward difference approximation is used to approximate the first derivative of $\mathcal{C}$, and all other spatial derivates are approximated using central difference

approximations:

$$\begin{aligned}&\frac{\mathcal{C}_i^{j+1}-\mathcal{C}_i^{j}}{\Delta t}+v_i\left(\frac{\mathcal{C}_i^{j+1}-\mathcal{C}_{i-1}^{j+1}}{\Delta\xi}\right)-\frac{D}{\left(L^{j+1}\right)^2}\left(\frac{\mathcal{C}_{i-1}^{j+1}-2\mathcal{C}_i^{j+1}+\mathcal{C}_{i+1}^{j+1}}{\left(\Delta\xi\right)^2}\right)\\&+\frac{\mathcal{C}_i^{j+1}}{\eta q_i^{j+1}\left(L^{j+1}\right)^2}\left\{\left(\frac{f_{i-1}^{j+1}-2f_i^{j+1}+f_{i+1}^{j+1}}{\left(\Delta\xi\right)^2}\right)\right.\\&\left.-\frac{1}{q_i^{j+1}}\left(\frac{q_{i+1}^{j+1}-q_{i-1}^{j+1}}{\Delta\xi}\right)\left(\frac{f_{i+1}^{j+1}-f_{i-1}^{j+1}}{\Delta\xi}\right)\right\}=Z\left(\mathcal{C}_i^{j+1}\right),\qquad i=2,\ldots,n-1.\end{aligned}\tag{87}$$

where

$$v_i=\frac{1}{\eta q_i^{j+1}\left(L^{j+1}\right)^2}\left(\frac{f_{i+1}^{j+1}-f_{i-1}^{j+1}}{2\Delta\xi}\right)-\frac{\xi}{L^{j+1}}\left(\frac{L^{j+1}-L^{j}}{\Delta t}\right),\qquad i=2,\ldots,n-1.\tag{88}$$

Similarly, forward difference approximations are used when $v_i<0$. The boundary condition at $\xi=0$ is

$$0=\mathcal{C}_2-\mathcal{C}_1.\tag{89}$$

Numerical exploration revealed that a ghost node was necessary to solve $\partial\mathcal{C}/\partial\xi=0$ at $\xi=1$. The use of a ghost node ensured that the numerical solution of the continuum model agreed with the solution of the discrete model. The ghost node is placed outside the right domain boundary at $i=n+1$. A central difference approximation is applied to the zero–flux boundary condition to obtain $\mathcal{C}_{n+1}^{j+1}=\mathcal{C}_{n-1}^{j+1}$. To incorporate the ghost node, Equation (79) is factorised as

$$\frac{\partial\mathcal{C}}{\partial t}+v\frac{\partial\mathcal{C}}{\partial\xi}+\frac{\mathcal{C}}{\eta L^2}\frac{\partial}{\partial\xi}\left(\frac{1}{q}\frac{\partial f}{\partial\xi}\right)-\frac{D}{L^2}\frac{\partial^2\mathcal{C}}{\partial\xi^2}=Z\left(\mathcal{C}\right).\tag{90}$$

Backward and central difference approximations are used to discretise Equation (90) as

$$\frac{\mathcal{C}_n^{j+1}-\mathcal{C}_n^{j}}{\Delta t}+v_n\left(\frac{\mathcal{C}_n^{j+1}-\mathcal{C}_{n-1}^{j+1}}{\Delta\xi}\right)-\frac{D}{\left(L^{j+1}\right)^2}\left(\frac{\mathcal{C}_{n-1}^{j+1}-2\mathcal{C}_n^{j+1}+\mathcal{C}_{n+1}^{j+1}}{\Delta\xi^2}\right)\tag{91}$$

$$+\frac{\mathcal{C}_n^{j+1}}{\eta\left(L^{j+1}\right)^2}\frac{1}{\Delta\xi}\left\{\frac{1}{q_n^{j+1}}\left(\frac{f_n^{j+1}-f_{n-1}^{j+1}}{\Delta\xi}\right)-\frac{1}{q_{n-1}^{j+1}}\left(\frac{f_n^{j+1}-f_{n-1}^{j+1}}{\Delta\xi}\right)\right\}=Z\left(\mathcal{C}_n^{j+1}\right).\tag{92}$$

Substituting $\mathcal{C}_{n+1}^{j+1}=\mathcal{C}_{n-1}^{j+1}$ and factorising gives the boundary condition at $\xi=1$ as

$$\begin{aligned}&\frac{\mathcal{C}_n^{j+1}-\mathcal{C}_n^{j}}{\Delta t}+v_n\left(\frac{\mathcal{C}_n^{j+1}-\mathcal{C}_{n-1}^{j+1}}{\Delta\xi}\right)-\frac{D}{\left(L^{j+1}\right)^2}\left(\frac{2\mathcal{C}_{n-1}^{j+1}-2\mathcal{C}_n^{j+1}}{\left(\Delta\xi\right)^2}\right)\\&+\frac{\mathcal{C}_n^{j+1}}{\eta\left(L^{j+1}\right)^2}\frac{1}{\Delta\xi}\left(\frac{1}{q_n^{j+1}}-\frac{1}{q_{n-1}^{j+1}}\right)\left(\frac{f_n^{j+1}-f_{n-1}^{j+1}}{\Delta\xi}\right)=Z\left(\mathcal{C}_n^{j+1}\right).\end{aligned}\tag{93}$$

where

$$v_n=\frac{1}{\eta q_n^{j+1}\left(L^{j+1}\right)^2}\left(\frac{f_n^{j+1}-f_{n-1}^{j+1}}{\Delta\xi}\right)-\frac{\xi}{L^{j+1}}\left(\frac{L^{j+1}-L^{j}}{\Delta t}\right).\tag{94}$$

Equation (77) is discretised as

$$f_i^{j+1} = k\left(\mathcal{C}_i^{j+1}\right)\left(\frac{1}{q_i^{j+1}} - a\left(\mathcal{C}_i^{j+1}\right)\right), \qquad i = 1, \ldots, n, \tag{95}$$

and substituted into Equations (84)–(94) to form a non-linear system of equations.

We solve Equations (84)–(86) for q_i^{j+1} and Equations (87)–(94) for $\mathcal{C}_i^{j+1}$ using the Newton-Raphson method [62]. At each Newton-Raphson iteration, Equation (82) is used to update the position of the free boundary as

$$L^{j+1} = L^j + \frac{\Delta t}{\eta q_n^{j+1} L^j}\frac{f_n^{j+1} - f_{n-1}^{j+1}}{\Delta \xi}. \tag{96}$$

Newton-Raphson iterations are continued until the norm of the difference between successive solution estimates of q_i^{j+1} and $\mathcal{C}_i^{j+1}$ are both less than a specified tolerance, ϵ. To ensure all numerical results are grid–independent, $\Delta\xi = 10^{-3}$, $\Delta t = 10^{-3}$ and $\epsilon = 10^{-8}$. All linear systems are solved using the Thomas algorithm [61].

C Case study 1: Homogeneous tissue

In Section 3.1, we examine a homogeneous tissue with $N = 20$ cells, one chemical species, $\boldsymbol{\mathcal{C}}(x,t) = \mathcal{C}_1(x,t)$, and no chemical source, $Z_1(\mathcal{C}_1) = 0$. Figure 7(a)–(b) demonstrates that $q(x,t)$, $\mathcal{C}_1(x,t)$ and $L(t)$ become constant as $t \to \infty$. To obtain expressions for the long time behaviour of $q(x,t)$, $\mathcal{C}_1(x,t)$ and $L(t)$, the total number of cells, N, and total number of chemical particles, P, are computed as,

$$N = \int_0^{L(t)} q(x,t)\,\mathrm{d}x, \qquad P = \int_0^{L(t)} \mathcal{C}_1(x,t)\,\mathrm{d}x. \tag{97}$$

Using Equation (97), $N = q(x,0)L(0)$ and $P = \mathcal{C}_1(x,0)L(0)$. As the tissue relaxes, the cells elongate such that the length of individual cells approaches the cell resting length. Thus, $q(x,t)$, $\mathcal{C}_1(x,t)$ and $L(t)$ become constant,

$$\lim_{t\to\infty} q(x,t) = \frac{1}{a}, \qquad \lim_{t\to\infty} \mathcal{C}_1(x,t) = \frac{P}{Na}, \qquad \lim_{t\to\infty} L(t) = Na. \tag{98}$$

Figure 7(c)–(d) shows that the average cell density, $\tilde{q}(x,t)$, and the average chemical concentration, $\tilde{\mathcal{C}}_1(x,t)$, approach the limits stated in Equation (98) as $t \to \infty$.

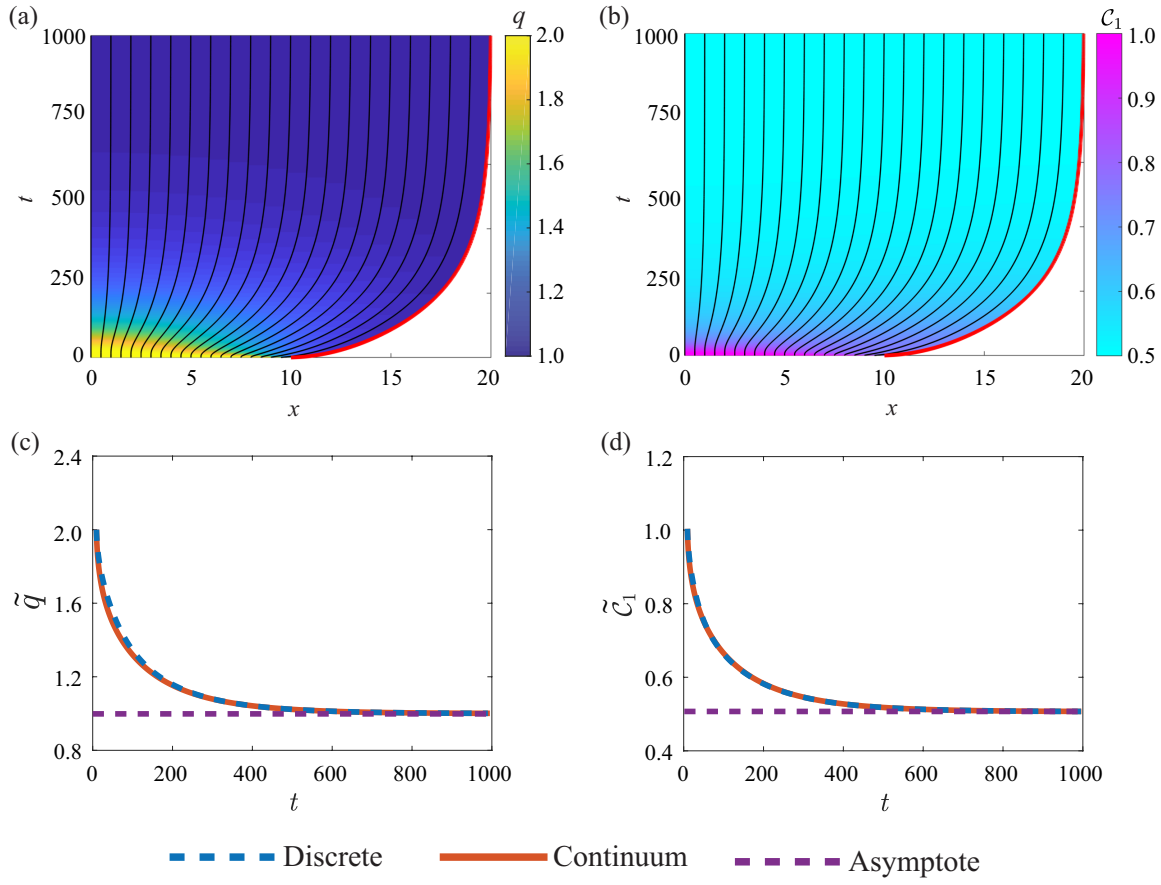

Figure 7: Homogeneous tissue consisting of one chemical species where $Z_1(\mathcal{C}_1) = 0$ and $a = k = D_1 = \eta = 1$. Characteristic diagrams in (a)–(b) illustrate the position of cell boundaries where the free boundary is highlighted in red. The colour in (a)–(b) represents $q(x,t)$ and $\mathcal{C}_1(x,t)$ respectively. Discrete and continuum solutions for the average cell density, $\tilde{q}(x,t)$, and the average chemical concentration, $\tilde{\mathcal{C}}_1(x,t)$ are compared in (c)–(d) respectively. The purple line in (c)–(d) shows the asymptotic behaviour of $\tilde{q}(x,t) = 1/a$ and $\tilde{\mathcal{C}}_1(x,t) = P/(Na)$ respectively.

D Case study 2: Rac–Rho pathway

To investigate the Rac–Rho pathway, we let $\boldsymbol{\mathcal{C}}(x,t) = \{\mathcal{C}_1(x,t), \mathcal{C}_2(x,t)\}$ such that $\mathcal{C}_1(x,t)$ represents the concentration of RhoA and $\mathcal{C}_2(x,t)$ represents the concentration of Rac1. Figure 8 compares the discrete and continuum solutions relating to Figure 5.

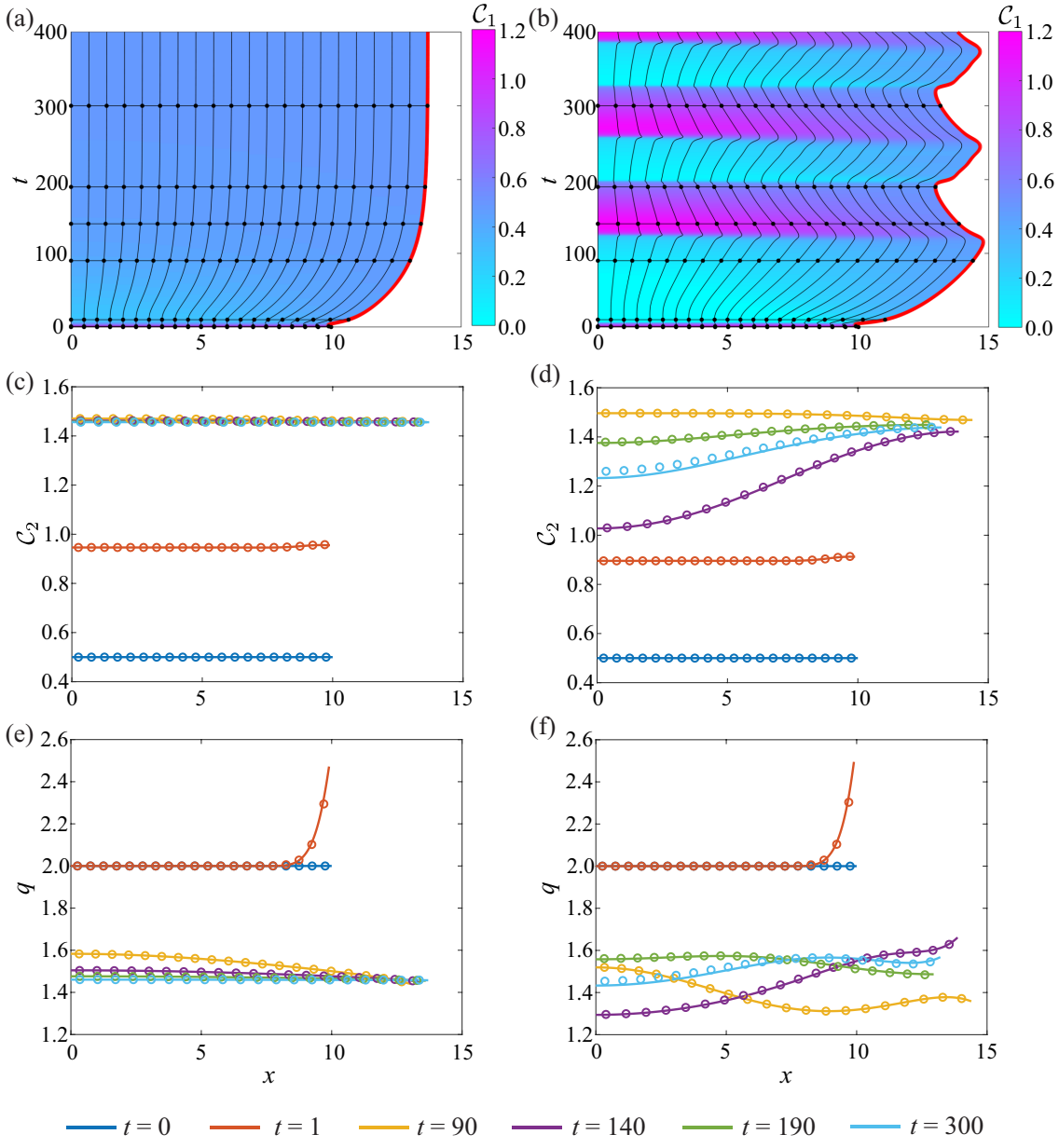

Figure 8: 1D tissue dynamics for the interaction of RhoA and Rac1. (a),(c),(e) correspond to non-oscillatory system where $\hat{\beta} = 1$ and (b),(d),(f) relate to an oscillatory system where $\hat{\beta} = 2.5$. Characteristic diagrams in (a)–(b) illustrate the behaviour of $\mathcal{C}_1(x,t)$ where the free boundary is highlighted in red. The black horizontal lines indicate times at which $\mathcal{C}_2(x,t)$ and $q(x,t)$ snapshots are shown in (c)–(d) and (e)–(f) respectively. In (c)–(f), the discrete and continuum solutions are compared as the dots and solid line respectively for $t = 0, 1, 90, 140, 190, 300$. In both systems, $a = l_0 - \phi\mathcal{C}_1^p / (G_h^p + \mathcal{C}_1^p)$, $k = 1 + 0.1\mathcal{C}_2$, $D_1 = D_2 = 1$ and $\eta = 1$. Parameters: $b_1 = b_2 = 1, \delta_1 = \delta_2 = 1, n = 3, p = 4, G_{1_T} = 2, G_{2_T} = 3, l_0 = 1, \phi = 0.65, G_h = 0.4$.

D.1 Single cell model

To investigate the influence of the mechanobiological coupling on cellular dynamics, a discrete computational framework is used to model a single cell [12,33]. We let $\mathbf{C}(t) = \left\{C^{(1)}(t), C^{(2)}(t)\right\}$ where $C^{(1)}(t)$ represents RhoA and $C^{(2)}(t)$ represents Rac1. As only a single cell is of interest, $\mathbf{C}(t)$ is not indexed with a subscript (Figure 9). Mechanobiological coupling is introduced such that the cell resting length, $a = a\left(\mathbf{C}\right)$, and the cell stiffness, $k = k\left(\mathbf{C}\right)$, depend on the chemical family, $\mathbf{C}(t)$.

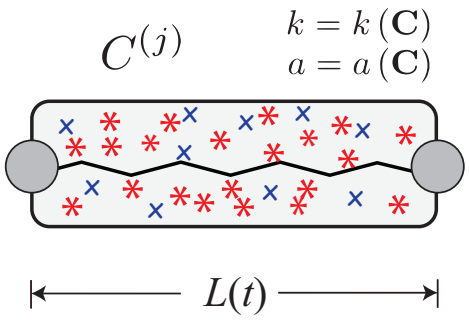

Figure 9: Schematic of a single cell with length $L(t)$. The mechanical cell properties, a and k, depend on the family of chemical signals, $\mathbf{C}(t) = \left\{C^{(1)}(t), C^{(2)}(t)\right\}$.

We model the cell as an overdamped, mechanical spring [8,39] such that $\mathbf{C}(t)$ tends to decrease as the cell expands, and tends to increase as the cell compresses. Thus, the governing equations are,

$$\frac{\mathrm{d}L}{\mathrm{d}t} = -\varepsilon\left(L - a\left(\mathbf{C}\right)\right), \tag{99}$$

$$\frac{\mathrm{d}C^{(j)}}{\mathrm{d}t} = \underbrace{Z^{(j)}\left(\mathbf{C}\right)}_{\substack{\text{chemical}\\ \text{reactions}}} - \underbrace{\frac{C^{(j)}}{L}\frac{\mathrm{d}L}{\mathrm{d}t}}_{\substack{\text{changes in}\\ \text{cell length}}}, \tag{100}$$

where $L(t)$ is the cell length, $\varepsilon = 2k\left(\mathbf{C}\right)/\eta$ is the rate of contraction, η is the mobility coefficient and $Z^{(j)}\left(\mathbf{C}\right)$ governs the reactions between the chemical species within the cell [12]. For simplicity, the cell stiffness is chosen to be independent of $\mathbf{C}(t)$ such that ε is constant. The cell resting length is assumed to vary from a fixed value, l_0 [12]. By including a Hill function with amplitude ϕ, switch location G_{h} and power p, we assume RhoA shortens the resting cell length [12],

$$a\left(\mathbf{C}\right) = l_0 - \phi\frac{\left(C^{(1)}\right)^p}{G_{\mathrm{h}} + \left(C^{(1)}\right)^p}. \tag{101}$$

Equations (99) and (100) form a dynamical system. Phase planes are constructed to characterise the dependence of the system stability on the strength of the mechanobiological coupling. We used this analysis to inform our choice of model parameters in Section 3.2. The equilibrium points, $\bar{L}$ and $\bar{C}^{(j)}$, are determined by setting the time derivatives to zero such that $\bar{L} = a\left(\bar{\mathbf{C}}\right)$ and $Z^{(j)}\left(\bar{\mathbf{C}}\right) = 0$.

To investigate a single cell containing only RhoA, we consider [12]

$$Z^{(1)}\left(C^{(1)}\right) = \overbrace{\left(b + \underbrace{\gamma\frac{\left(C^{(1)}\right)^n}{1 + \left(C^{(1)}\right)^n}}_{\text{feedback loop}} + \underbrace{\beta\left(L(t) - a\left(C^{(1)}\right)\right)}_{\substack{\text{mechanobiological}\\ \text{coupling}}}\right)\left(G_{\mathrm{T}} - C^{(1)}\right)}^{\text{activation}} - \underbrace{\delta C^{(1)}}_{\text{deactivation}}, \tag{102}$$

where b is the basal activation rate, γ is rate of feedback activation, β governs the strength of the mechanobiological coupling, G_{T} is the total amount of active and inactive RhoA, and δ is the deactivation rate [12, 33]. By substituting $\bar{L} = a\left(\bar{\mathbf{C}}\right)$ into $Z^{(1)}\left(\bar{C}^{(1)}\right) = 0$, $\bar{C}^{(1)}$ is numerically computed as the roots of,

$$0 = (-b-\gamma+\delta)\left(\bar{C}^{(1)}\right)^{n+1} + (bG_{\mathrm{T}}+\delta G_{\mathrm{T}})\left(\bar{C}^{(1)}\right)^{n} + (-b+\delta)\,\bar{C}^{(1)} + bG_{\mathrm{T}}. \tag{103}$$

As Equation (103) is independent of β. Thus, we vary β to investigate how the system stability depends on the strength of the mechanobiological coupling (Figure 10). Phase planes are constructed using `quiver` in MATLAB [63] and trajectories are computed using `ode15s` in MATLAB [42] (Figure 10).

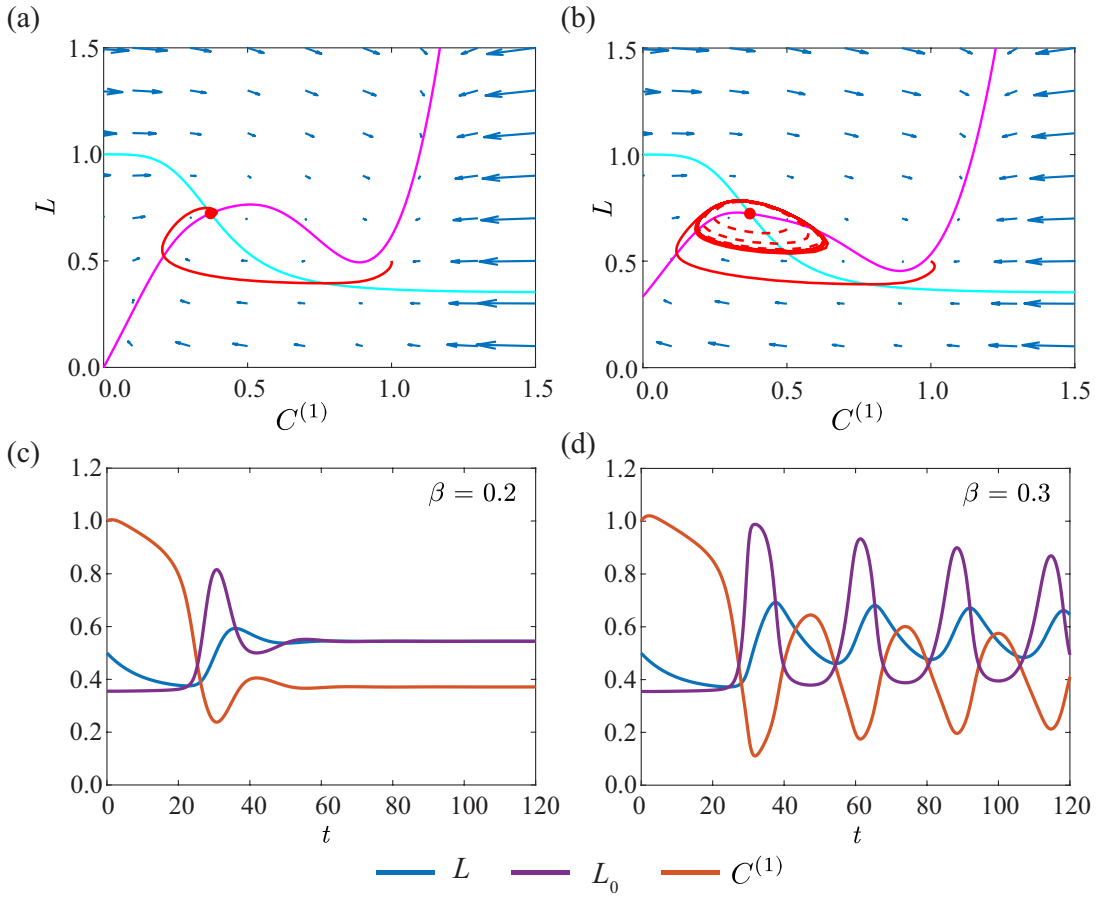

Figure 10: Dynamics of a single cell containing RhoA. (a),(c) corresponds to a non-oscillatory system where $\beta = 0.2$, and (b),(d) corresponds to an oscillatory system where $\beta = 0.3$. In (a)–(b), cyan represents the L nullcline and magenta represents the $C^{(1)}$ nullcline. The trajectory for $\left(C^{(1)}(0), L(0)\right) = (0.5, 1)$ is shown in red. In (b), the additional trajectory for $\left(C^{(1)}(0), L(0)\right) = (0.5, 0.65)$ is drawn as a dashed red line to demonstrate that all solutions exhibit oscillatory behaviour for $\beta = 0.3$. Parameters are: $b = 0.2, \gamma = 1.5, n = 4, p = 4, G_{\mathrm{T}} = 2, l_0 = 1, \phi = 0.65, G_{\mathrm{h}} = 0.4, \delta = 1, \varepsilon = 0.1$.

Figure 10(a),(c) demonstrates that the equilibrium point is stable when $\beta = 0.2$, and the cell exhibits non-oscillatory behaviour. By increasing the strength of the mechanobiological coupling to $\beta = 0.3$, a limit cycle arises which leads to continuous oscillations in $L(t)$ and $C^{(1)}(t)$ (Figure 10(b),(d)). Stability analysis reveals that the equilibrium point is unstable for $\beta = 0.3$. Thus, all solutions, regardless of the initial condition, exhibit oscillatory behaviour when $\beta = 0.3$ (Figure

10(b)).

To investigate how intracellular reactions between RhoA and Rac1 impact cell behaviour, we consider [12]

$$Z^{(1)}(\mathbf{C}) = \overbrace{\left(b_1 + \underbrace{\hat{\beta}\left(L(t) - a\left(C^{(1)}\right)\right)}_{\substack{\text{mechanobiological}\\ \text{coupling}}}\right)\frac{1}{1+\left(C^{(2)}\right)^n}\left(G_{1_\mathrm{T}} - C^{(1)}\right)}^{\text{activation}} - \underbrace{\delta_1 C^{(1)}}_{\text{deactivation}}, \tag{104}$$

$$Z^{(2)}(\mathbf{C}) = \underbrace{\frac{b_2}{1+\left(C^{(1)}\right)^n}\left(G_{2_\mathrm{T}} - C^{(2)}\right)}_{\text{activation}} - \underbrace{\delta_2 C^{(2)}}_{\text{deactivation}}. \tag{105}$$

Figure 11(a),(c) illustrates that when the mechanobiological coupling is weak, $\hat{\beta} = 1$, the equilibrium point is stable and the cell mechanically relaxes. By increasing the strength of the mechanobiological coupling to $\hat{\beta} = 2.5$, a limit cycle arises and the cell exhibits oscillatory behaviour (Figure 11(b),(d)).

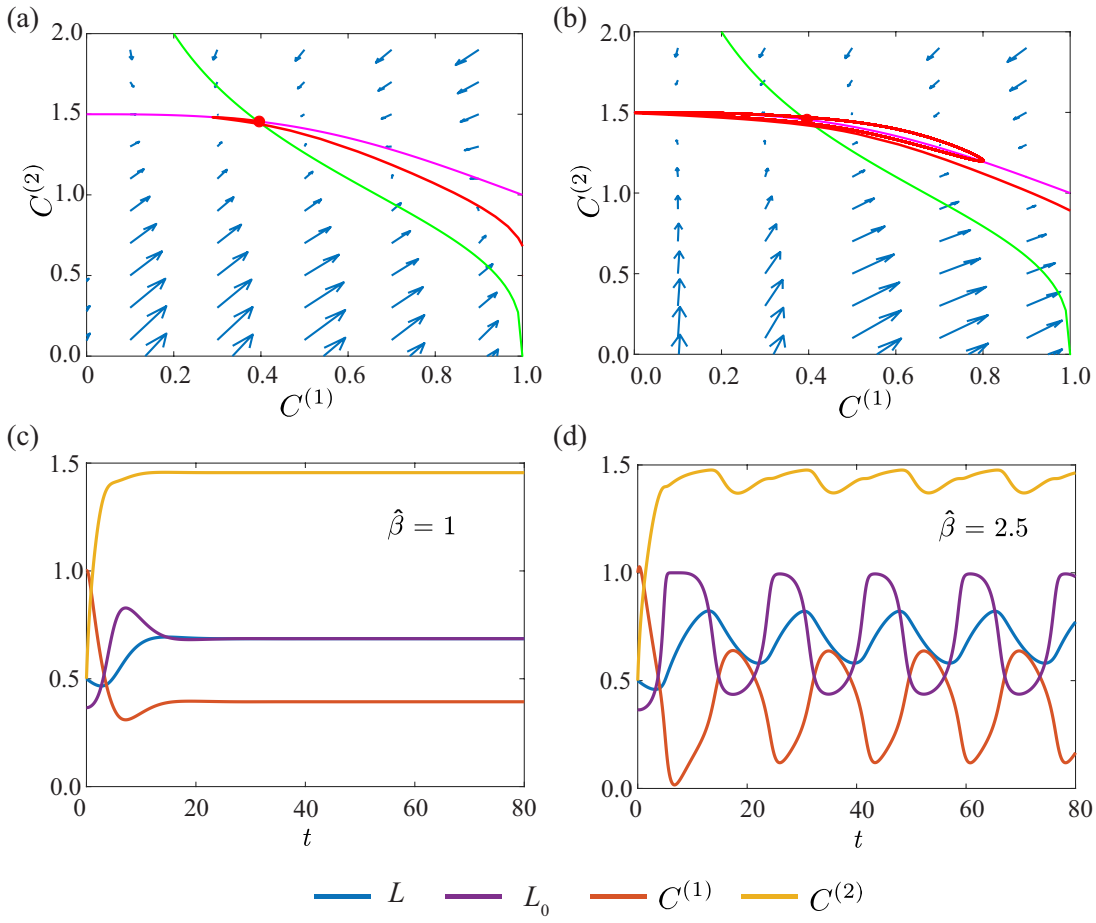

Figure 11: Reactions between RhoA and Rac1 in a single cell. (a),(c) corresponds to a non-oscillatory system where $\hat{\beta} = 1$, and (b),(d) corresponds to an oscillatory system where $\hat{\beta} = 2.5$. In (a)–(b), magenta represents the $C^{(1)}$ nullcline and green represents the $C^{(2)}$ nullcline. The trajectory for $\left(L(0), C^{(1)}(0), C^{(2)}(0)\right) = (0.5, 1, 0.5)$ in shown in red. Parameters: $b_1 = b_2 = 1, \delta_1 = \delta_2 = 1, n = 3, p = 4, G_{1_\mathrm{T}} = 2, G_{2_\mathrm{T}} = 3, l_0 = 1, \phi = 0.65, G_\mathrm{h} = 0.4, \varepsilon = 0.1$.

E Case study 3: Activator–inhibitor patterning

Section 3.3 considers an activator–inhibitor system with $\boldsymbol{\mathcal{C}}(x,t) = \{\mathcal{C}_1(x,t), \mathcal{C}_2(x,t)\}$ where $\mathcal{C}_1(x,t)$ is the activator and $\mathcal{C}_2(x,t)$ is the inhibitor. Figure 12 illustrates the long time behaviour of Figure 6(b),(d) and shows two distinct activator peaks evolve as $t \to \infty$ for $d > d_c$. Thus, unlike [25, 26], we do not observe continuous peak splitting.

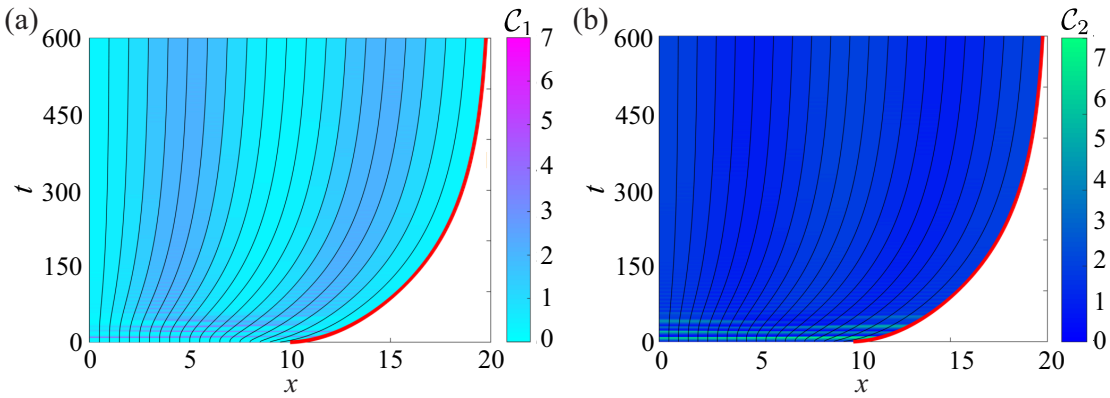

Figure 12: The evolution of spatial–temporal patterns in a homogeneous tissue with Schnakenberg dynamics where $D_1 = 0.5$ and $D_2 = 5$ such that $d > d_c$. (a) illustrates the behaviour of the activator, $\mathcal{C}_1(x,t)$, and (b) illustrates the behaviour of the inhibitor, $\mathcal{C}_2(x,t)$. Parameters are as in Figure 6.

References

[1] Fozard JA, Byrne HM, Jensen OE, King JR. 2010. Continuum approximations of individual–based models for epithelial monolayers. *Mathematical Medicine and Biology.* **27**, 39–74. (doi: 10.1093/imammb/dqp015).

[2] Guillot C, Lecuit T. 2013. Mechanics of epithelial tissue homeostasis and morphogenesis. *Science.* **340**, 1185–1189. (doi: 10.1126/science.1235249).

[3] Xu GK, Liu Y, Li B. 2015. How do changes at the cell level affect the mechanical properties of epithelial monolayers? *Soft Matter.* **11**, 8782–8788. (doi: 10.1039/c5sm01966d).

[4] Dasbiswas K, Hannezo E, Gov NS. 2018. Theory of epithelial cell shape transitions induced by mechanoactive chemical gradients. *Biophysical Journal.* **114**, 968–977. (doi: 10.1016/j.bpj.2017.12.022).

[5] Baker RE, Parker A, Simpson MJ. 2019. A free boundary model of epithelial dynamics. *Journal of Theoretical Biology.* **481**, 61–74. (doi: 10.1016/j.jtbi.2018.12.025).

[6] Murphy RJ, Buenzli PR, Baker RE, Simpson MJ. 2019. An individual–based mechanical model of cell movement in heterogeneous tissues and its coarse–grained approximation. *Proceedings of the Royal Society A: Mathematical, Physical and Engineering Sciences.* **475**, 20180838. (doi: 10.1101/485276).

[7] Murphy RJ, Buenzli PR, Baker RE, Simpson, MJ. 2020. Mechanical cell competition in heterogeneous epithelial tissues. To appear, *Bulletin of Mathematical Biology.* Available on bioRxiv:869495. (doi: 10.1101/869495).

[8] Murray PJ, Edwards CM, Tindall MJ, Maini PK. 2009. From a discrete to a continuum model of cell dynamics in one dimension. *Physical Review E: Statistical, Nonlinear, and Soft Matter Physics.* **80**, 031912. (doi: 10.1103/PhysRevE.80.031912).

[9] Murray PJ, Edwards CM, Tindall MJ, Maini PK. 2012. Classifying general non-linear force laws in cell–based models via the continuum limit. *Physical Review E: Statistical, Nonlinear, and Soft Matter Physics.* **85**, 021921. (doi: 10.1103/PhysRevE.85.021921).

[10] Lorenzi T, Murray PJ, Ptashnyk M. 2019. From individual–based mechanical models of multi-cellular systems to free–boundary problems. Preprint on arXiv:1903.06590.

[11] Smith AM, Baker RE, Kay D, Maini PK. 2012. Incorporating chemical signalling factors into cell–based models of growing epithelial tissues. *Journal of Mathematical Biology.* **65**, 441–463. (doi: 10.1007/s00285-011-0464-y).

[12] Zmurchok C, Bhaskar D, Edelstein-Keshet L. 2018. Coupling mechanical tension and GTPase signalling to generate cell and tissue dynamics. *Physical Biology.* **15**, 046004. (doi: 10.1088/1478-3975/aab1c0).

[13] Zmurchok C, Collette J, Rajagopal V, Holmes WR. 2020. Membrane tension can enhance adaptation to maintain polarity of migrating cells. Preprint on bioRxiv:2020.04.01.020289. (doi: 10.1101/2020.04.01.020289).

[14] Boocock D, Hino N, Ruzickova N, Hirashima T, Hannezo E. Theory of mechano–chemical patterning and optimal migration in cell monolayers. Preprint on bioRxiv:096479. (doi: 10.1101/2020.05.15.096479).

[15] Osborne JM, Fletcher AG, Pitt-Francis JM, Maini PK, Gavaghan DJ. 2017. Comparing individual–based approaches to modelling the self–organization of multicellular tissues. *PLoS Computational Biology*. **13**, e1005387. (doi: 10.1371/journal.pcbi.1005387).

[16] Evans ND, Oreffo RO, Healy E, Thurner PJ, Man YH. 2013. Epithelial mechanobiology, skin wound healing, and the stem cell niche. *Journal of the Mechanical Behaviour of Biomedical Materials*. **28**, 397–409. (doi: 10.1016/j.jmbbm.2013.04.023).

[17] Fletcher AG, Cooper F, Baker RE. 2017. Mechanocellular models of epithelial morphogenesis. *Philosophical Transactions of the Royal Society B: Biological Sciences*. **372**, 20150519. (doi: 10.1098/rstb.2015.0519).

[18] Friedman A. 2015. Free boundary problems in biology. *Philosophical Transactions of the Royal Society A: Mathematical, Physical and Engineering Sciences*. **373**, 20140368. (doi: 10.1098/rsta.2014.0368).

[19] Serra-Picamal, X, Conte V. Vincent R, Anon E, Tambe DT, Bazellieres E, Butler JP, Fredberg JJ, Trepat X. 2012. Mechanical waves during tissue expansion. *Nature Physics*. **8**, 628–634. (doi: 10.1038/NPHYS2355).

[20] El-Hachem M, McCue SW, Wang J, Yihong D, Simpson MJ. 2019. Revisiting the Fisher–Kolmogorov–Petrovsky–Piskunov equation to interpret the spreading–extinction dichotomy. *Proceedings of the Royal Society A: Mathematical, Physical and Engineering Sciences.* **475**, 20190378. (doi: 10.1098/rspa.2019.0378).

[21] Du Y, Lin Z. 2010. Spreading-vanishing dichotomy in the diffusive logistic model with a free boundary. *SIAM Journal on Mathematical Analysis*. **42**, 377–405. (doi: 10.1137/090771089).

[22] Simpson MJ, Landman KA, Newgreen DF. 2006. Chemotactic and diffusive migration on a nonuniformly growing domain: numerical algorithm development and applications. *Journal of Computational and Applied Mathematics*. **192**, 282–300. (doi: 10.1016/j.cam.2005.05.003).

[23] Simpson MJ, Sharp JA, Baker RE. 2015. Survival probability for a diffusive process on a growing domain. *Physical Review E: Statistical, Nonlinear, and Soft Matter Physics*. **91**, 042701. (doi: 10.1103/PhysRevE.91.042701).

[24] Simpson MJ, Baker RE. 2015. Exact calculations of survival probability for diffusion on growing lines, disks, and spheres: the role of dimension. *The Journal of Chemical Physics*. **143**, 094109. (doi: 10.1063/1.4929993).

[25] Maini PK, Woolley TE, Baker RE, Gaffney EA, Lee SS. 2012. Turing's model for biological pattern formation and the robustness problem. *Interface Focus*. **2**, 487–496. (doi: 10.1098/rsfs.2011.0113).

[26] Crampin EJ, Hackborn WW, Maini PK. 2002. Pattern formation in reaction–diffusion models with non-uniform domain growth. *Bulletin of Mathematical Biology*. **64**, 747–769. (doi: 10.1006/bulm.2002.0295).

[27] Crampin EJ, Gaffney EA, Maini PK. 1999. Reaction and diffusion on growing domains: scenarios for robust pattern formation. *Bulletin of Mathematical Biology.* **61**, 1093–1120. (doi: 10.1006/bulm.1999.0131).

[28] Crampin EJ, Gaffney EA, Maini PK. 2002. Mode–doubling and tripling in reaction–diffusion patterns on growing domains: a piecewise linear model. *Journal of Mathematical Biology.* **44**, 107–128. (doi: 10.1007/s002850100112).

[29] Pathmanathan P, Cooper J, Fletcher AG, Mirams G, Murray PJ, Osborne JM, Pitt-Francis J, Walter A, Chapman SJ. 2009. A computational study of discrete mechanical tissue models. *Physical Biology.* **6**, 036001. (doi: 10.1088/1478-3975/6/3/036001).

[30] Armstrong NJ, Painter KJ, Sherratt JA. 2006. A continuum approach to modelling cell–cell adhesion. *Journal of Theoretical Biology.* **243**, 98–113. (doi: 10.1016/j.jtbi.2006.05.030).

[31] Murphy RJ, Buenzli PR, Baker RE, Simpson MJ. 2020. Travelling waves in a free boundary mechanobiological model of an epithelial tissue. To appear, *Applied Mathematics Letters.* Available on arXiv:2005.13925.

[32] Dalwadi MP, Waters SL, Byrne HM, Hewitt IJ. 2020. A mathematical framework for developing freezing protocols in the cryopreservation of cells. *SIAM Journal on Applied Mathematics.* **80**, 657–689. (doi: 10.1137/19M1275875).

[33] Bui J, Conway DE, Heise RL, Weinberg SH. 2019. Mechanochemical coupling and junctional forces during collective cell migration. *Biophysical Journal.* **117**, 170–183. (doi: 10.1016/j.bpj.2019.05.020).

[34] Holmes WR, Park J, Levchenko A, Edelstein-Keshet L. 2017. A mathematical model coupling polarity signalling to cell adhesion explains diverse cell migration patterns. *PLoS Computational Biology.* **13**, e1005524. (doi: 10.1371/journal.pcbi.1005524).

[35] Byrne KM, Monsefi N, Dawson JC, Degasperi A, Bukowski-Wills J, Volinsky N, Dobrzynski M, Birtwistle MR, Tsyganov MA, Kiyatkin A, Kida K, Finch AJ, Carragher NO, Kolch W, Nguyen LK, von Kriegsheim A, Kholodenko BN. 2016. Bistability in the Rac1, PAK, and RhoA signalling network drives actin cytoskeleton dynamics and cell motility switches. *Cell Systems.* **2**, 38–48. (doi: 10.1016/j.cels.2016.01.003).

[36] Ridley AJ. 2001. Rho family proteins: coordinating cell responses. *Trends in Cell Biology.* **11**, 471–477. (doi: 10.1016/s0962-8924(01)02153-5).

[37] Guilluy C, Garcia-MataR, Burridge K. 2011. Rho protein crosstalk: another social network? *Trends in Cell Biology.* **21**, 718–726. (doi: 10.1016/j.tcb.2011.08.002).

[38] Samuel MS, Lopez JI, McGhee EJ, Croft DR, Strachan D, Timpson P, Munro J, Schroder E, Zhou J, Brunton VG, Barker N, Clevers H, Sansom OJ, Anderson KI, Weaver VM, Olson MF. 2011. Actomyosin–mediated cellular tension drives increased tissue stiffness and β-catenin activation to induce epidermal hyperplasia and tumour growth. *Cancer Cell.* **19**, 776–791. (doi: 10.1016/j.ccr.2011.05.008).

[39] Matsiaka OM, Penington CJ, Baker RE, Simpson MJ. 2017. Continuum approximations for lattice–free multi–species models of collective cell migration. *Journal of Theoretical Biology.* **422**, 1–11. (doi: 10.1016/j.jtbi.2017.04.009).

[40] Painter KJ, Sherratt JA. 2003. Modelling the movement of interacting cell populations. *Journal of Theoretical Biology.* **225**, 327–339. (doi: 10.1016/S0022-5193(03)00258-3).

[41] Yates CA, Baker RE, Erban R, Maini PK. 2012. Going from microscopic to macroscopic on non-uniform growing domains. *Physical Review E: Statistical, Nonlinear, and Soft Matter Physics.* **86**, 21921. (doi: 10.1103/PhysRevE.86.021921).

[42] MathWorks `ode15s`. Retrieved from https://au.mathworks.com/help/matlab/ref/ode15s.html in June 2020.

[43] Simpson MJ. 2020. Critical length for the spreading–vanishing dichotomy in higher dimensions. *ANZIAM Journal.* 1–15. (doi: 10.1017/S1446181120000103).

[44] Holmes WR, Edelstein-Keshet L. 2016. Analysis of a minimal Rho–GTPase circuit regulating cell shape. *Physical Biology.* **13**, 046001. (doi: 10.1088/1478-3975/13/4/046001).

[45] Zmurchok C, Holmes WR. 2020. Simple Rho GTPase dynamics generate a complex regulatory landscape associated with cell shape. *Biophysical Journal.* **118**, 1438–1454. (doi: 10.1016/j.bpj.2020.01.035).

[46] Abreu-Blanco MT, Verboon JM, Parkhurst SM. 2014. Coordination of Rho family GTPase activities to orchestrate cytoskeleton responses during cell wound repair. *Current Biology.* **24**, 144–155. (doi: 10.1016/j.cub.2013.11.048).

[47] Clayton NS, Ridley AJ. 2020. Targeting Rho GTPase signalling networks in cancer. *Frontiers in Cell and Developmental Biology.* **8**, 222. (doi: 10.3389/fcell.2020.00222).

[48] Haga RB, Ridley AJ. 2016. Rho GTPases: regulation and roles in cancer cell biology. *Small GTPases.* **7**, 207–221. (doi: 10.1080/21541248.2016.1232583).

[49] Sabass B, Gardel ML, Waterman CM, Schwarz US. 2008. High resolution traction force microscopy based on experimental and computational advances. *Biophysical Journal.* **94**, 207–220. (doi: 10.1529/biophysj.107.113670).

[50] Pertz O, Hahn KM. 2004. Designing biosensors for Rho family proteins–deciphering the dynamics of Rho family GTPase activation in living cells. *Journal of Cell Science.* **117**, 1313–1318. (doi: 10.1242/jcs.01117).

[51] Houk A, Jilkine A, Mejean C, Boltyanskiy R, Dufresne E, Angenent S, Altschuler S, Wu F, Weiner O. 2012. Membrane tension maintains cell polarity by confining signals to the leading edge during neutrophil migration. *Cell.* **148**, 175–188. (doi: 10.1016/j.cell.2011.10.050).

[52] Sharma S, Santiskulvong C, Rao J, Gimzewski JK, Dorigo O. 2014. The role of Rho GTPase in cell stiffness and cisplatin resistance in ovarian cancer cells. *Integrative Biology.* **6**, 611–617. (doi: 10.1039/c3ib40246k).

[53] Murray J. 2002. *Mathematical Biology.* New York: Springer.

[54] Wentz JM, Mendenhall AR, Bortz DM. Pattern formation in the longevity–related expression of heat shock protein-16.2 in Caenorhabditis elegans. *Bulletin of Mathematical Biology.* **80**, 2669–2697. (doi: 10.1007/s11538-018-0482-7).

[55] Turing A. 1952. The chemical basis of morphogenesis. *Philosophical Transactions of the Royal Society B: Biological Sciences.* **237**, 37–72. (doi: 10.1098/rstb.1952.0012).

[56] Kondo S, Asai R. 1995. A reaction–diffusion wave on the skin of the marine angelfish Pomacanthus. *Nature*. **376**, 765–768. (doi: 10.1038/376765a0).

[57] Anguige K, Schmeiser C. 2009. A one–dimensional model of cell diffusion and aggregation, incorporating volume filling and cell-to-cell adhesion. *Journal of Mathematical Biology*. **58**, 395. (doi: 10.1007/s00285-008-0197-8).

[58] Codling EA, Plank MJ, Benhamou S. 2008. Random walk models in biology. *Journal of the Royal Society Interface*. **5**, 813–834. (doi: 10.1098/rsif.2008.0014).

[59] El-Hachem M, McCue SW, Simpson MJ. 2020. A sharp–front moving boundary model for malignant invasion. *Physica D: Nonlinear Phenomena*. **412**, 132639. (doi: 10.1016/j.physd.2020.132639).

[60] Provenzano PP, Keely PJ. 2011. Mechanical signalling through the cytoskeleton regulates cell proliferation by coordinated focal adhesion and Rho GTPase signalling. *Journal of Cell Science*. **124**, 1195–1205. (doi: 10.1242/jcs.067009).

[61] Wang H, Anderson M. 1982. I*ntroduction to Groundwater Modeling Finite Difference and Finite Element Methods.* San Diego: Academic Press.

[62] Kelley C. 2003. *Solving Nonlinear Equations with Newton's Method*. Philadelphia: Society for Industrial and Applied Mathematics.

[63] MathWorks `quiver`. Retrieved from https://au.mathworks.com/help/matlab/ref/quiver.html in June 2020.